



Federal University of ABC
Center for Engineering, Modeling and Applied Social Sciences
Graduate Program in Mechanical Engineering

Three-dimensional axisymmetric study of turbulent swirling flow for gas-liquid separation

Rodrigo Vidal Cabral

Santo André - SP, December 2021

Rodrigo Vidal Cabral

Three-dimensional axisymmetric study of turbulent swirling flow for gas-liquid separation

Master's thesis submitted to the Graduate Program in Mechanical Engineering (concentration area: Transport Phenomena), as part of the requirements for obtaining the Master's Degree in Mechanical Engineering.

Federal University of ABC – UFABC
Center for Engineering, Modeling, and Applied Social Sciences
Graduate Program in Mechanical Engineering

Supervisor: Prof. Dr. André Damiani Rocha
Co-supervisor: Prof. Dr. Sungki Jung

Santo André - SP
December 2021

Cabral, Rodrigo Vidal

Three-dimensional axisymmetric study of turbulent swirling flow for gas-liquid separation/ Rodrigo Vidal Cabral. – Santo André - SP, December 2021-
74 p. : il.

Supervisor: Prof. Dr. André Damiani Rocha

Supervisor: Prof. Dr. Sungki Jung

Dissertação (Mestrado) – Federal University of ABC – UFABC
Center for Engineering, Modeling, and Applied Social Sciences
Graduate Program in Mechanical Engineering, December 2021.

1. Computer fluid dynamics. 2. swirl flow. 3. turbulent flow. I. Prof. Dr. André Damiani Rocha. II. Prof. Dr. Sungki Jung. III. Programa de pós-graduação em engenharia mecânica. IV. Two-dimensional study of turbulent flow with axially induced swirl for gas-liquid separation

CDU 02:141:005.7

Rodrigo Vidal Cabral

Three-dimensional axisymmetric study of turbulent swirling flow for gas-liquid separation

Master's thesis submitted to the Graduate Program in Mechanical Engineering (concentration area: Transport Phenomena), as part of the requirements for obtaining the Master's Degree in Mechanical Engineering.

Prof. Dr. André Damiani Rocha
Supervisor

Prof. Dr. Sungki Jung
Co-supervisor

Prof. Dr. —
Member of the evaluation committee

Prof. Dr. —
Member of the evaluation committee

Santo André - SP
December 2021

I dedicate this work to my parents, Isabel and Cabral, who always provided the best conditions for my academic and personal development, besides all the immeasurable affection. To my brother Diogo for his companionship and brotherhood. To my partner Isabella, for her understanding and unrestricted support.

Acknowledgements

To my supervisor Prof. Dr. André Damiani Rocha for the friendship and knowledge shared in this journey. To my co-supervisor Prof. Dr. Sungki Jung for the knowledge added to the work and to my education. To the professors who were part of my academic and professional training. To my friends and colleagues who somehow helped me in this constant process of learning life.

To CAPES (Coordenação de Aperfeiçoamento de Pessoal de Nível Superior) for the financial support for this research work.

“Science works on the frontier between knowledge and ignorance. We’re not afraid to admit what we don’t know – there’s no shame in that. The only shame is to pretend that we have all the answers.”
(Neil deGrasse Tyson)

Resumo

São diversas as aplicações que utilizam a mecânica do escoamento com giro, tem-se como alguns exemplos na engenharia a otimização de queima em câmaras de combustão, separadores ciclônicos, intensificadores para troca de calor e turbomáquinas. Os separadores ciclônicos de entrada axial são demandados na produção de óleo e gás devido a sua disposição *in-line* e *design* compacto. Os fenômenos presente no escoamento com giro de um hidrociclone axial é objeto de estudo desta dissertação de mestrado tendo como objetivo a identificação, e redução dos fenômenos adversos para a separação líquido-gás. Utilizou-se uma abordagem via CFD por meio de um software comercial Ansys Fluent. O domínio computacional é bidimensional e discretizado por uma malha quadrilátera com seção constante. Realizou-se estudos laminar e turbulento para validação do modelo utilizado, ambos monofásico e isotérmico. Explorou-se os campos de velocidade axial e velocidade tangencial, campo de pressão, intensidade e decaimento do giro. Outro objeto de estudo foi adição de uma cauda aerodinâmica a jusante do separador como forma de atenuar os efeitos adversos do escoamento. Coeficiente de arrasto, tensão de cisalhamento e coeficiente de pressão foram explorados numericamente na cauda, além da queda de pressão induzida no escoamento. O terceiro estudo realizado foi da dinâmica de uma partícula de gás dispersa em uma fase contínua de líquido, variando o diâmetro das partículas. Os resultados obtidos atingiu a expectativa de validação do modelo adotado e apresentou dados fundamentais para continuidade do estudo.

Palavras-chaves: escoamento com giro, escoamento turbulento, dinâmica dos fluidos computacional, separador ciclônico de entrada axial.

Abstract

There are several applications that use the flow mechanics with swirl, some examples in engineering are the optimization of burning in combustion chambers, cyclonic separators, intensifiers for heat exchange and turbomachine. Axial inlet cyclonic separators are required in the production of oil and gas due to their in-line disposition and compact design. The phenomena present in the swirling flow of an axial hydrocyclone is the object of study of this master's thesis with the objective of identify and reduce adverse phenomena for liquid-gas separation. An approach via CFD was used using commercial software Ansys Fluent. The computational domain is two-dimensional and discretized by a quadrilateral mesh with a constant section. Laminar and turbulent studies were carried out to validate the model used, both single-phase and isothermal. The fields of axial velocity and tangential velocity, pressure field, intensity and swirl decay were explored. Another object of study was the addition of an aerodynamic tail downstream of the separator as a way to mitigate the adverse effects of the flow. Drag coefficient, shear stress and pressure pressure were explored numerically in the tail, in addition to the pressure drop induced in the flow. The third study carried out was the dynamics of a particle of gas dispersed in a continuous phase of liquid, varying the diameter of the particles. The results obtained reached the expectation of validation of the adopted model and presented fundamental results for the continuity of the study.

Keywords: swirling flow, turbulent flow, computational fluid dynamics, axial inlet cyclonic separator.

List of Figures

Figure 1 – Typical facilities of an oil production unit (ARNOLD, 2007).	2
Figure 2 – Typical facilities of a gas treatment plant (ARNOLD, 2007).	3
Figure 3 – Three-phase separation tanks: (a) horizontal and (b) vertical (Aong, 2020).	3
Figure 4 – Different types of cyclones for gas-liquid separation (HUANG et al., 2018).	4
Figure 5 – Axial inlet cyclonic separator (SAVREE, 2020).	5
Figure 6 – (a) Tangential inlet cyclones (HOFFMANN; STEIN, 2008) and (b) axial inlet (TYVOLD, 2015).	10
Figure 7 – Rankine Vortex (LIMA, 2011)	12
Figure 8 – Swirl Region Classification (STEENBERGEN; VOSKAMP, 1998)	15
Figure 9 – Coordinate System (Source: Personal collection)	23
Figure 10 – Variation of ϕ with time (Source:)	26
Figure 11 – Convective and diffusive flow in the control volume (Source: Moukalled et al. (2016))	33
Figure 12 – Numerical method (Source: Anderson, J. D. (1995))	34
Figure 13 – Pressure-Based solution method (Source: Adapted from Ansys (2018))	37
Figure 14 – Study construction(Source:Personal collection)	38
Figure 15 – Flow solution steps (Source: Personal collection)	38
Figure 16 – Computational domain (Source: Personal collection)	39
Figure 17 – Smoothing between control volumes (Source: Personal collection)	40
Figure 18 – Orthogonality (Source: Personal collection)	40
Figure 19 – Boundary layer (Source: Personal collection)	41
Figure 20 – Mesh refinement near the wall (Source: Personal collection)	42
Figure 21 – Results Measurement Guidelines (Source: Personal collection)	44
Figure 22 – Convergence of the solution in steady state (Source: Personal collection)	45
Figure 23 – Convergence of the solution in transient (Source: Personal collection)	45
Figure 24 – Computer domain Ayinde (Source: Ayinde (2010))	47
Figure 25 – Axial velocity profile (Source: Ayinde (2010))	49
Figure 26 – Tangential velocity profile (Source: Ayinde (2010))	49
Figure 27 – Swirl number decay (Source: Ayinde (2010))	50
Figure 28 – Static pressure on the wall (Source: Personal collection)	51
Figure 29 – (a) Axial velocity profile (b) Tangential velocity profile (Source: Dirkzwager (1996))	52
Figure 30 – Tangential velocity (Source: personal collection	54
Figure 31 – Tangential velocity field (Source: personal collection)	54
Figure 32 – Axial velocity (Source: personal collection	55

Figure 33 – Axial velocity field (Source: personal collection)	56
Figure 34 – Axial velocity field (Source: personal collection)	56
Figure 35 – Aerodynamic tail (Source: personal collection)	59
Figure 36 – Cases (Source: personal collection)	60
Figure 37 – Aerodynamic tail (Source: personal collection)	61
Figure 38 – Pressure coefficient (Source: personal collection)	63
Figure 39 – Shear stress (Source: personal collection)	63
Figure 40 – Boundary layer separation region (Source: personal collection)	64

List of Tables

Table 1 – Model closure constants $k-\varepsilon$	29
Table 2 – Model closure SSG	31
Table 3 – Model closure rate of dissipation	31
Table 4 – Grid Convergence Index for tangencial velocity $Re = 4.9 \cdot 10^4$	42
Table 5 – Grid Convergence Index for drag coefficient $Re = 4.9 \cdot 10^4$	42
Table 6 – Boundary conditions	43
Table 7 – Properties	43
Table 8 – Numerical residuals	44
Table 9 – Swirl number	57
Table 10 – Cases Perfis Power Series	60
Table 11 – Drag coefficient values per case	62

List of abbreviations and acronyms

CFD	Computer Fluid Dynamics
RANS	Reynolds Averaged Navier-Stokes
LES	Large Eddy Simulation
DNS	Direct Numerical Simulation
RSM	Reynolds Stress Model
CAPES	Coordenação de Aperfeiçoamento de Pessoal de Nível Superior
Re	Reynolds Number
S	Swirl number
PVC	Processing Vortex Core
VBD	Vortex Breakdown
UDF	User Define Fuction
DPM	Discrete Phase Model
SIMPLE	Semi-Implicity Method for Linked Equations
GCI	GridConvergence Index

List of symbols

δ	Greek letter delta minuscule
Δ	Greek letter delta capitals
ε	Greek letter Epsilon
ρ	Greek letter rho
θ	Greek letter theta
Γ	Greek Gamma letter
π	Greek letter pi
∂	Differential symbol
∇	Gradient operator symbol
ϕ	Greek letter phi
u	Axial velocity
v	Radial velocity
w	Tangential velocity
r	Radius
D	Diameter
L	Length

Contents

1	INTRODUCTION	1
1.1	Motivation	5
1.2	Objective	6
1.3	Contribution of the dissertation	6
1.4	Dissertation Structure	6
2	LITERATURE REVIEW	9
2.1	Introduction	9
2.2	Cyclones	9
2.2.1	Art history	10
2.3	Flow properties with swirl	11
2.4	Laminar flow with swirl	12
2.5	Turbulent Flow with Swirl	14
2.5.1	Application of CFD in turbulent cyclone studies	16
2.6	Axial Hydrocyclone	18
2.7	Turbulent two-phase (liquid-gas) flow applied to separation	20
3	NUMERICAL MODELING	23
3.1	Introduction	23
3.2	Mathematical formulation	23
3.2.1	Laminar modelling	24
3.2.2	Turbulent modeling	25
3.2.3	Reynolds Average	26
3.2.4	K- ϵ Model	29
3.2.5	Reynolds Stress Model	29
3.2.6	Wall function	31
3.2.7	Swirl number	33
3.3	Numerical method	33
3.3.1	Discretization of the governing equations	34
3.3.2	Temporal Discretization	35
3.3.3	Coupling pressure and velocity	36
3.3.4	Study methodology	37
3.3.5	Steps	38
3.4	Computational domain	39
3.4.1	Computational mesh	39
3.4.2	Mesh independence study	41

3.4.3	Boundary conditions and pre-processing	42
3.4.4	Convergence	43
4	NUMERICAL VALIDATION	47
4.1	Introduction	47
4.2	Laminar validation with swirl	47
4.3	Turbulent validation with swirl	50
4.3.1	Axial static pressure	51
4.3.2	Velocity field	52
4.3.2.1	Tangential velocity	53
4.3.2.2	Axial velocity	55
4.3.3	Swirl number	56
5	TAIL AERODYNAMIC ANALYSIS	59
5.1	Introduction	59
5.2	Aerodynamic Profile	59
5.3	Theoretical Foundation	60
5.4	Simulations	62
5.5	Results and selection	62
6	DYNAMICS OF A GAS PARTICLE	65
6.1	Introduction	65
6.2	Mathematical formulation	65
6.3	Computer modeling of the trajectory	66
7	RESULTS AND DISCUSSIONS	67
8	CONCLUSIONS AND SUGGESTIONS FOR FUTURE WORK	69
	Conclusão e Trabalhos Futuros	69
	REFERENCES	71

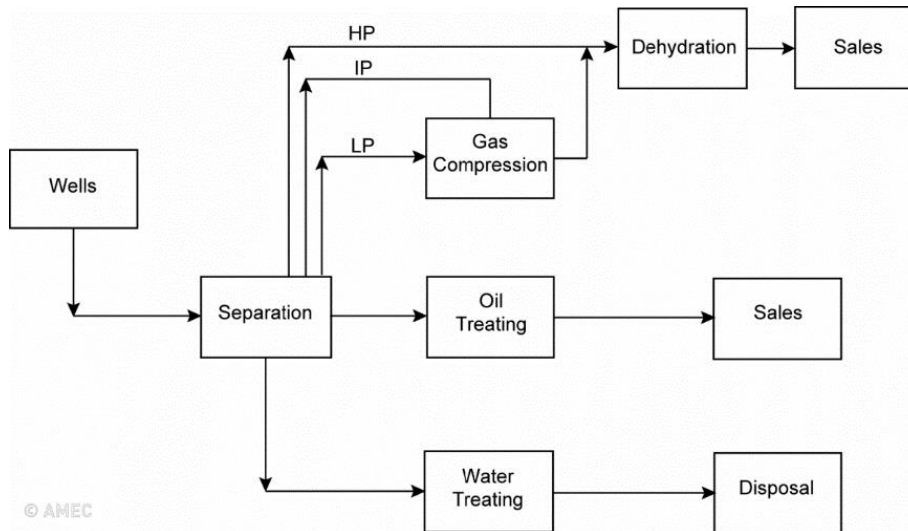
1 Introduction

The Brazilian oil and gas production market has increasingly stood out on the international scene, especially after the discovery of the pre-salt layer, which led the country to be part of global production networks, the so-called GPRs, the backbone and central nervous system of the world economy. In Brazil, proven oil resources are estimated at 15 billion barrels, which puts it in second place in South America, just behind Venezuela. Almost 95% of these resources are located offshore, 80% of which are off the coast of Rio de Janeiro State (SCHOLVIN et al., 2020). In addition, Brazil also has the second largest natural gas reserves in South America, which are primarily located in the Campos Basin. During the process of regulating the oil wells, Petrobras was required by the Brazilian government to have a broad participation of national services, workforce and technology, certified and controlled by the ANP (National Petroleum Agency). One of the measures established by the agency was the mandatory national headquarters of foreign companies that intend to explore the national oil fields, leading to the creation of the technological park in Rio de Janeiro. This measure boosted the entry of foreign companies and strengthened the relationship with the national ones in order to adapt to the existing technologies and local conditions, i.e., the specific requirements of the pre-salt, in which the exploration is carried out in ultra-deep waters. These associations generated knowledge dissemination and innovation effects that may even boost the internationalization of Brazilian companies, promoting technologies developed initially for local applications and that may have global reach.

In general, reservoirs are located in ultra-deep layers of the sea, the result of the long geological process of formation. The permeabilization of the porous rocks allowed, over time, the deposition of elements essential for energy production, such as crude oil and natural gas, in addition to brackish water from the sea. Throughout the productive life of an oil field there is usually simultaneous production of fluids and solids. Oil or gas wells produce a mixture of hydrocarbon gas, condensate, or oil. Water with dissolved minerals, usually including a large amount of salt, is also produced. Other gases, including nitrogen, carbon dioxide (CO_2) and possibly hydrogen sulfide (H_2S) can also be present. Regarding solids, reservoir sand, dirt, scale and corrosion products from piping are normally produced during the process. As the economic interest is only in the production of hydrocarbons (oil and gas), there is a need to use equipment designed to perform the primary processing of fluids. The primary processing of fluids includes the following steps: separation of oil, gas and water with impurities in suspension; treatment or conditioning of hydrocarbons so that they can be transferred to the refineries; water treatment for re-injection or disposal (TRIGGIA, 2001).

A primary processing plant can be simple or complex depending on the type of fluid produced and the techno-economic feasibility of the primary processing plant. The Figure 1 shows the typical facilities of an oil production unit.

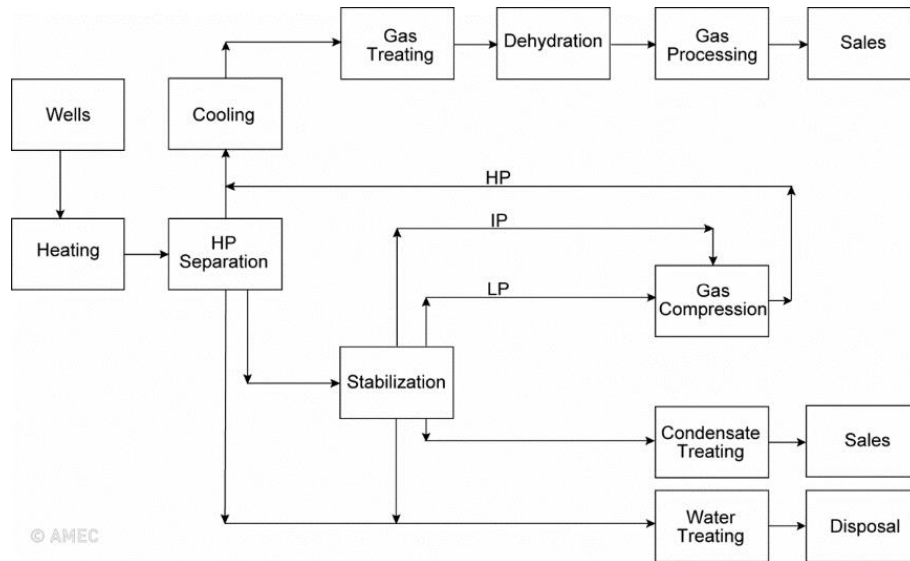
Figure 1 – Typical facilities of an oil production unit (ARNOLD, 2007).



Gas treatment is necessary to remove impurities and contaminants, remove liquids and solids that are still present after the separation process in the tank, and prepare the gas to the buyers' requirements. Treatment of the oil is also necessary to bring it up to sales standard. This standard involves, among other requirements, the maximum allowable amount of oil, salt, and impurities. No separation is perfect, and there is always a little water in the oil. No separation is perfect and there is always some water in the oil. The water content in oil can range from less than 1% to more than 20% of the oil by volume. To remove as much water as possible from the oil, the oil is processed through a treatment system that usually provides heat to reduce viscosity and large settling sections that allow separation of water and oil over time and may also provide an electrostatic grid to promote coalescence of the water droplets. Water treatment is equally important in fluid processing because the water can be reinjected into the reservoir to increase oil recovery or disposed of in compliance with environmental laws. Each of the treatment processes presented above involves different techniques and various equipment to achieve the goal of fluid processing. The focus of this study is related to the acceleration of the gas-liquid separation process. The figure 2 shows the block diagram of a typical gas treatment plant.

The separator provides a place for any liquid to deposit from the gas. The separator pressure is set above the pipeline pressure so that the gas can go through the necessary cooling, treating, dehydration, and gas processing - each with some pressure drop - and reach the required pipeline pressure. The gas-liquid separation process usually occurs in a separation tank into which the well fluid flows allowing the gas, oil, and water to separate due to the action of gravity. A separator can be two-phase, separating the gas from the

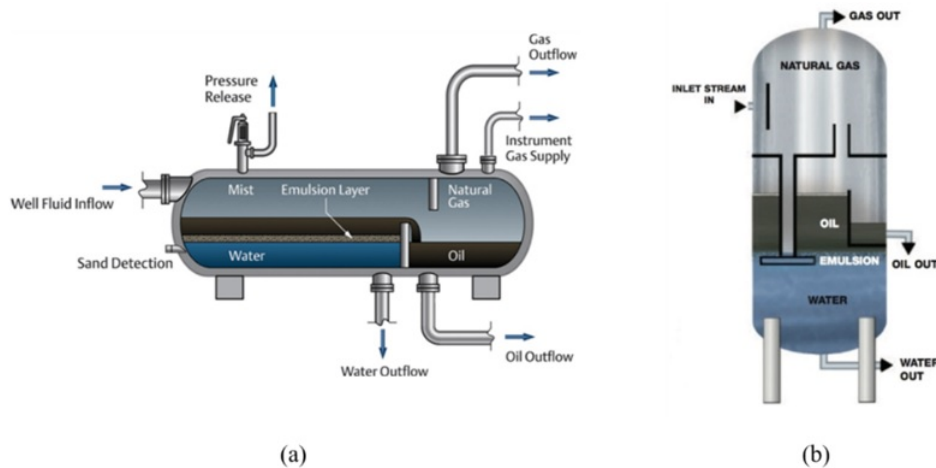
Figure 2 – Typical facilities of a gas treatment plant (ARNOLD, 2007).



liquids, or three-phase, separating the gas, oil, and water. The Figure 3 shows two types of three-phase gravity separation tanks: horizontal and vertical. The main problem is the size of the separator tanks used today. To achieve a large separation capacity the tanks need to be of large dimensions, which increases the weight and space occupied and consequently increases the cost of the processing facilities.

The separation process can be accelerated using centrifugal separation, which can have an effect a hundred times greater than gravity (SLOT, 2013). This type of equipment is known as a cyclone. In this case, the less dense phase will be forced by the centrifugal field to migrate toward the center while the more dense phase is forced to move toward the wall. Subsequent to segregation, the phases can be extracted by different extraction devices.

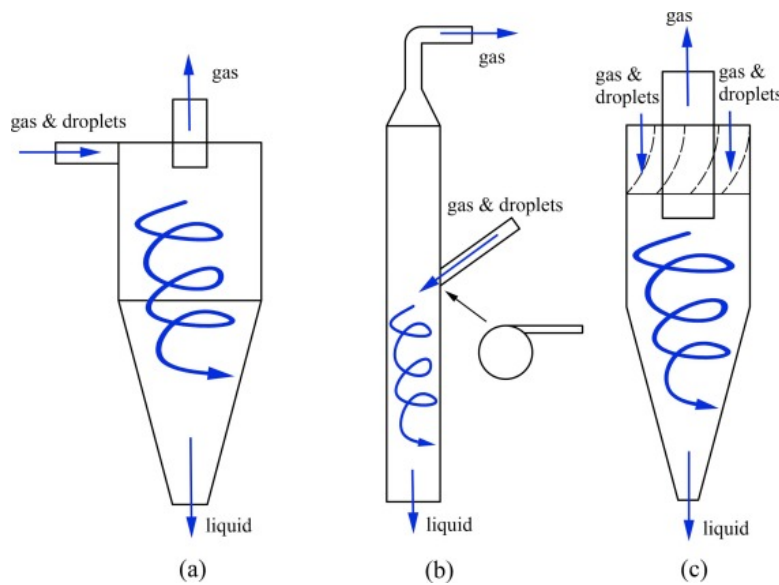
Figure 3 – Three-phase separation tanks: (a) horizontal and (b) vertical (Aong, 2020).



The figure 4 shows the most commonly used cyclone types in gas-liquid separation.

The most commonly used type of cyclone is the Stairmand cyclone (YANG et al., 2015) and (HOEKSTRA, 2000), shown in figure 4, which has a tangential inlet, a conical section through which the denser phase exits (underflow) and an exit through which the less dense phase exits (overflow). The figure 4b, shows the GLCC (Gas-Liquid Cylindrical Cyclone). The GLCC also has tangential inlet, but the separation chamber is cylindrical. A third type is the axial inlet type, as shown in the figure 4c. The characteristic as of these cyclones is that they are of the reverse flow type and the gas flows in the opposite direction of the liquid phase.

Figure 4 – Different types of cyclones for gas-liquid separation (HUANG et al., 2018).

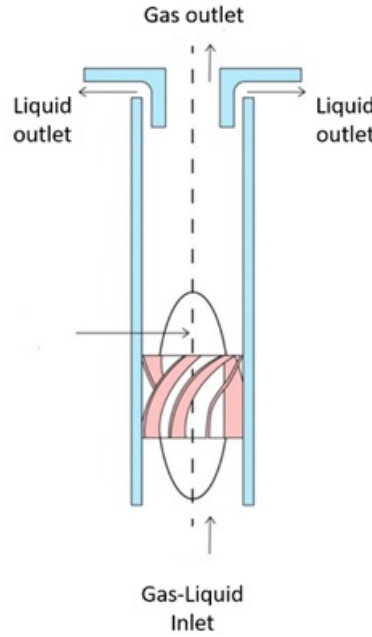


The axial inlet cyclone may have a cylindrical body, in which case both gas and liquid flow in the same direction, as shown in the figure 5.

This type of cyclone is more compact when compared to the tangential inlet cyclone and takes advantage of being able to be installed "in-line" with the production pipe, as shown in the figure 5. This feature has made this device recognized as an "inline separator". Besides being compact, the axial inlet cyclone is static, which lowers maintenance costs, leads to a lower level of instrumentation, control and monitoring. The reduction in operating costs extends the period when production is economically favorable providing increased oil and gas recovery and the economic potential of the field. A disadvantage of the axial inlet cyclone is the possibility of bubble breakage due to high shear stresses and turbulence effects, which hinders phase segregation.

Turbulent flow with swirl is essentially three-dimensional and transient leading to often complex numerical modeling, raising the computational cost. Using turbulent viscosity models to express Reynolds stresses in terms of averaged quantities is not suitable for high-swing flow, where the current lines are curved (POPE, 2000). The asymmetry of the flow violates the turbulent viscosity hypothesis that the shear stress and velocity gradient

Figure 5 – Axial inlet cyclonic separator (SAVREE, 2020).



have the same direction (KITOH, 1991). Various sources of turbulence, such as strain rates, are not represented by turbulent viscosity models. Furthermore, the assumption of isotropic turbulence causes shear stresses and radial diffusion of the momentum to be overestimated (MURPHY et al., 2007). This problem can be circumvented by using the Reynolds Strain Model or RSM (Reynolds Stress Model). The model provides 6 independent Reynolds stress equations for the closure of the problem. One of the advantages of this model is that the Reynolds stress production terms can be represented exactly. In the RSM model the strain rates associated with the curvature and asymmetry of the flow, both of which occur in swirling flow, are incorporated into the terms representing the turbulence production (HANJALIC, 2018). Furthermore, the flow in the axial separator is two-phase, with a complex topology. Solving all the details of the flow would be more computationally expensive than for single-phase turbulent flow.

Thus, the study performed in this dissertation considers single-phase, two-dimensional flow. The accuracy of this simplification is verified later. The trajectory of a fluid gas particle being charged by the flow is evaluated, using an Euler-Lagrangian approach, in order to obtain the separation length.

1.1 Motivation

The main motivation of this work is the wide use of cyclones in different areas of engineering, aiming the separation of phases. Specifically, the gas-liquid separation is important because of the pre-salt reserves that have light oils with large amounts of CO_2 . It is of interest to oil and gas operators to have a virtual laboratory, obtainable through

numerical simulations, that will allow them to refine and improve the efficiency of this type of separator.

In this study, attention is focused on the turbulent flow with swirl induced from fixed vane swirl generating element (SGE). Since the flow is simplified to a two-dimensional model, the SGE is not part of the computational domain. Considering a dispersed flow where the gas is the dispersed component and the oil the continuous phase, one will have the gas flowing through the center of the pipe and the oil near the wall. Finally, it is intended to obtain the optimal tail geometry.

1.2 Objective

The objective of this dissertation is to study numerically, using a commercial computational fluid dynamics tool (Ansys Fluent ®), the turbulent single-phase flow with swirl downstream of the SGE. The velocity field (axial, radial and tangential components), the pressure field and the swirl decay due to the viscous effect are investigated. The results of the simplified 2D model are compared with experimental results presented by [Dirkzwager \(1996\)](#). It is also desired to identify the length required for phase segregation considering a gas-liquid dispersion, through an Euler-Langrangean approach. The numerical results of the trajectory of a gas bubble will be compared with a simplified segregation model.

1.3 Contribution of the dissertation

The development of compact axial inlet separators is the current research topic in the group coordinated by Prof. André Damiani Rocha. For the first time in the group, two-dimensional modeling of turbulent, single-phase, axially induced swirling flow is investigated using computational fluid dynamics techniques. Cyclone performance is strongly dependent on geometric and flow characteristics. The study of single-phase flow will reveal the behavior of the axial, radial and tangential velocity components which is essential for the construction of a segregation model. In this context, the present MSc dissertation seeks to contribute to the development of a compact, in-line gas-liquid separator.

1.4 Dissertation Structure

This dissertation is structured in 6 chapters, with the following content:

- Chapter 2: Literature review

The literature on cyclones, swirling flow, turbulent swirling flow, and two-phase liquid-gas flows is presented. Mainly modeling forms and review of the most used

models in the literature are presented, such as the RANS model (Reynolds Averaged Navier-Stokes) for turbulence modeling and swirl flow characteristics with CFD application.

- Chapter 3: Numerical and Computational Modeling

The numerical and computational modeling of the study to be developed is presented, separating it into a single-phase and two-phase study using the finite volume method, briefly described. The numerical methods used, the boundary conditions, the validation of mesh independence and other parameters used in the simulations are presented in this chapter.

- Chapter 4: Numerical Validation

This chapter presents the methodologies used to validate the laminar and turbulent computational modeling. The mesh independence criteria are also presented in this section.

- Chapter 5: Aerodynamic Analysis

Aerodynamic modeling of the hydrocyclone tail is presented in this chapter.

- Chapter 6: Kinetics of a Particle

This chapter gives the mathematical formulation of the trajectory of a dispersed gas particle in the continuous liquid phase.

- Chapter 7: Results and Discussion

The results obtained from numerical simulations and their analysis are presented. The study for the choice of the optimal tail geometry aiming at the reduction of recirculation regions, with lower drag, low pressure drop and maximum swirl number, influential properties for separation effects, is also presented. Finally, a simplified study of the dynamics of a dispersed gas particle in a continuous liquid phase is presented.

- Conclusion

The conclusion is presented as a closing of the study and the main points to be developed in future work.

- Appendix

Supplementary information fundamental to understanding the study is attached in the appendix.

2 Literature review

2.1 Introduction

Swirling flows are widespread in engineering in different applications, which makes their study paramount for development in areas such as separation processes, combustion chambers, turbomachinery, and pollution control devices. Specifically in heat transfer, swirling flow is used to increase turbulence in order to enhance convective heat exchange in heat exchangers, for example. Swirl in the flow can be induced when it is desired for its application or it is necessary to suppress it when its formation is undesired.

This chapter presents a review of the studies presented in the literature regarding the characteristics of flows with swirl, modeling, CFD applications, comparisons between numerical and experimental results, two-phase liquid-gas applications, and theories of quantification of swirl.

2.2 Cyclones

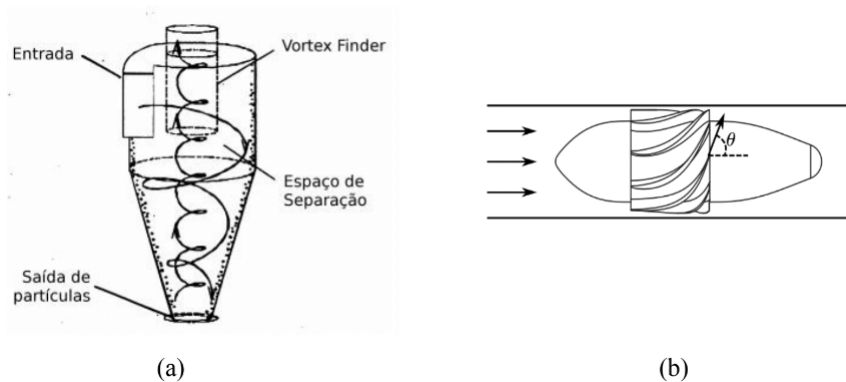
There are several types of cyclonic separators that are classified according to phase separation:

- Gas/Solid
- Gas/Liquid
- Liquid/Solid
- Liquid/Liquid

As much as the physics contained in each combination is similar, there are differences. Due to the higher viscous forces the liquid cyclone has lower turbulent properties, although the interfacial relationship between the phases can cause emulsions in liquid-liquid applications. Gas cyclones, on the other hand, have the advantage of a greater density difference, although there is the gas-liquid emulsion that forms foams. For cyclones applied to solid separation there is less influence of the separation effects, but they are subject to a greater wear of the whole apparatus. There is also the classification according to the flow entrance, geometry of the separation tube and extraction form of the segregated phase (CAMPEN, 2014).

- Inlet of the flow: There is the tangential inlet flow, where the flow enters through one or more tubes connected tangentially to the cyclone, in case of multiple inlets, they are distributed equidistantly on the circumference. In the axial inlet, we usually have a static element with vanes that accelerates and imposes rotation components to the flow. In the picture 6 illustrates the two forms of cyclones according to their input.

Figure 6 – (a) Tangential inlet cyclones (HOFFMANN; STEIN, 2008) and (b) axial inlet (TYVOLD, 2015).



- Tube geometry: In the conical form there is a reduction in the diameter of the separation tube. In the cylindrical shape, there is no reduction in the diameter of the separation tube, generally used in compact cyclones of axial application.
- Form of extraction: there is the counter-current configuration where the heavy phase exits downstream of the flow and the light phase upstream of the flow, usually found in tangential inlet cyclones. The other alternative is co-current as both exits are positioned downstream of the flow.

2.2.1 Art history

The first patented cyclone for application in phase separation occurred in 1891 (SVAROVSKI, 1984), and were used in mining processes and applied in power generation, the textile industry, and the chemical industry. These applications required the separation of solid particles dispersed in a liquid or gas. Around 1980 the first cyclones for oil-water mixing were developed at the University of Southampton by Smyth, Thew e Colman (1984). One of the first applications of these, then called hydrocyclones, was in offshore wells in Bass Strait between Tasmania and Australia, as described by Hayes et al. (1985).

The use of axial hydrocyclones to separate two liquids is still rare in industry, in general (NIEUWSSTADT; DIRKZWAGNER, 1995), (DIRKZWAGER, 1996) and (DELFO; DIRKZWAGER, 1998). A critical aspect of this separation occurs when the

densities of the fluids are close, as, for example, occurs when dealing with oil-water dispersions. Aiming to better understand the fluid-dynamic behavior of the flow in an axial hydrocyclone, [Rocha \(2013\)](#) and [Rocha, Bannwart e Ganzarolli \(2015\)](#) developed a new axial hydrocyclone. The authors performed numerical studies using CFD techniques and the results of the simulations provided important information for building the hydrocyclone and then performing the experiments. The axial hydrocyclone was experimented in single-phase flows, under laminar and turbulent regime conditions, varying the Reynolds number between 500 and 63,000. The velocity fields, pressure distribution and swirl intensity were the main parameters analyzed.

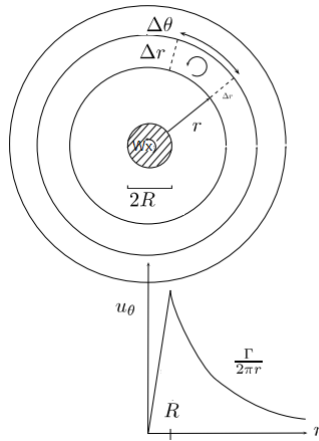
2.3 Flow properties with swirl

The swirling flow can be induced by different devices, with axial inlet, tangential inlet, helix-type generator, vane-formed guide rails, eave-type, through twisted strips, or through rotating tubes. They are generally applied to circular pipes and generate pressure drops that must be added to the design. When induced by the swirl generator device, the downstream flow acquires curved current lines, resulting from the tangential velocity field, the main characteristic of the swirling flow. To quantify its intensity the swirl number S is defined, which is given by the ratio between the tangential and axial velocity components. Throughout the flow the swirl intensity decays until it disappears, where the length to reestablish the flow without swirl depends on the inlet properties and pipe geometry ([GUPTA; LILLEY; SYRED, 1984](#)).

[Baker e Sayre \(1974\)](#) characterizes the swirling flow as a combination of vortical and axial motion. [Kitoh \(1991\)](#) presents the vorticity behavior for fixed-vane induced flow, where the vortex formed by the tangential component describes a behavior similar to Rankine's vortex. It is characterized by a forced vortex region where the tangential velocity increases with radial distance up to a maximum value and by the free vortex region where there is a decay of the tangential velocity radially to the pipe wall, as illustrated in figure 7. The vortex is divided into three main regions according to the variation of tangential velocity and by Reynolds' stresses, they are: the core region, where the flow has a rigid body rotation, in this region the flow is unstable and eddies are generated. The wall region, where the boundary layer predominates with a high velocity gradient. And the annular region, between the core and the boundary layer, called the free vortex where the flow is stable.

In a swirling flow there are vortices that characterize a rigid body, the fluid elements rotate around the origin axis as a rigid and rotating solid body, this analogy is associated with the forced vortex. The free vortex, on the other hand, is also called an irrotational vortex, except at the origin, where the vorticity is infinite. With this definition the Rankine

Figure 7 – Rankine Vortex (LIMA, 2011)



vortex can be called a forced-free vortex, because it combines the two characteristics to form the tangential velocity profile observed in real vortices. In the core there is a solid body rotation with sustained vorticity and outside the core the vortex is irrotational and the vorticity is infinite (KUNDU; COHEN, 2008).

One can also classify the swirling flow in pipes into two types: continuous swirl and swirl decay. Generally the continuous swirl is applied to flows where there is rotation of the pipe, maintaining the tangential velocity component throughout the length (OJO; ODUNFA; OYEWOLA, 2014). For the swirl decay classification, on the other hand, the tangential velocity component generated at the inlet is damped as the flow develops, usually downstream of swirl inducers, as is the case with cyclones.

The swirl decay is quantified from the swirl intensity of the flow. The swirl intensity, called swirl number (S), is a dimensionless number resulting from the ratio between angular momentum and axial momentum. In the literature there is a vast modeling of the swirl number, in this work we will use a combination of the studies presented by Syred e Beer (1974) and Kitoh (1991). The swirl number behaves as an exponential function of the axial distance, where experimental parameters were obtained to quantify the decay from an exponential curve (DIRKZWAGER, 1996) and (STEENBERGEN; VOSKAMP, 1998). In addition, Steenbergen (1995) presents in his study that the rate of decay of the swirl intensity is inversely proportional to the Reynolds number, thus, the higher the Reynolds number the greater the distance for total dissipation of the swirl, provided that the friction factor and shear stress are maintained for comparison purposes, because they are important parameters for the project.

2.4 Laminar flow with swirl

One of the first studies of laminar flow with swirl was developed by Talbot (1954) which performed an analytical and experimental study of the flow for low Reynolds numbers.

The analytical study showed that the decay of swirling flow in a pipe is exponential, i.e., the tangential velocity downstream of the flow exhibits exponential decay behavior in the direction of flow, furthermore, the decay rates are inversely proportional to the Reynolds number for the cases investigated where the Reynolds number was greater than 100.

Lavan, Nielsen e Fejer (1969), analytically investigated laminar, incompressible, swirling flow in a pipe consisting of two parts: a stationary pipe and a pipe rotating at a constant angular velocity. The authors obtained a linearized solution, valid for small Reynolds numbers, $0,4 \leq Re \leq 40$ and swirl numbers $4,74 \leq S \leq 22,45$. It was analyzed that when the fluid enters the tube containing the swirl generator, a reverse flow region is observed in the center of the tube and that the shear stress on the wall is higher than in a flow without swirl. A study of laminar flow with swirl using boundary layer analysis and finite difference method was developed by Kiya, Fukusaco e Arie (1971) with the objective of evaluating the inlet region of the flow in a circular section tube. The authors concluded that the length of the inlet region increases with increasing swirl velocity (tangential component), reaching 27% higher when compared to the flow without swirl. In addition, the authors also observed that the pressure drop decreases appreciably due to the presence of the swirl in the flow. Finally, the authors also identified that the decay rate is higher than in the rest of the pipe where the decay is exponential. Singh, Sinha e Aggarwal (1980) investigated the laminar, 2D axisymmetric flow with swirl in a constant circular cross section pipe using the combined asymptotic expansion method and verified three regions of the flow: (1) core region, called non-viscous core; (2) boundary layer and (3) upstream flow. For Reynolds numbers equal to 100 and 500, the authors concluded that: the increase in swirl velocity at the inlet implies the increase in vorticity as the flow develops in the core and this leads to the conclusion that the axial velocity increases in the core region. Silvester e Sleight (1984) in the numerical study of 2D laminar flow with swirl using variable primitive and proposes that the problem be used as a reference for calculating flow with swirl. Using Lavan, Nielsen e Fejer (1969) as a basis for comparison of results and varying Reynolds number between $2 \leq Re \leq 16$, the authors showed that the results of the numerical model showed good agreement when compared with the literature. A study of 3D laminar flow, symmetric to the central axis of the pipe, with swirl, incompressible and in permanent regime was investigated numerically by Ayinde (2010). Using specific boundary conditions at the inlet, from the developed profile for the axial velocity component and Rankine vortex for the tangential velocity component, for Reynolds numbers $80 \leq Re \leq 1800$, the authors investigated the decay of the swirl intensity as a function of Reynolds number and different velocity distributions at the inlet. The author concluded that the presence of flow with swirl distorts the developed axial velocity field and is gradually recovered as the tangential velocity is dissipated. Furthermore, the author identified that the decay of the swirl is exponential starting at 16D. Rocha, Bannwart e Ganzarolli (2017), numerically investigated the effects of boundary conditions for a 2D laminar incompressible flow in

a constant circular cross-section pipe of 50 mm diameter. The effects considered by the authors were: Reynolds number of the flow (790, 953 and 1283), deflection angle (15° , 30° , 45° and $63,5^\circ$) of the flow caused by the fixed vanes and the vane attachment thickness (5 mm and 10 mm). The authors identified that all boundary conditions affect the flow field and the swirl decay. In addition, the authors identified and characterized the reverse flow region in the center of the tube, which is associated with vortex breaking.

2.5 Turbulent Flow with Swirl

This section presents literature studies of turbulent flow with experimental swirl and numerical methods applied to CFD, the main objective of this dissertation.

The study of turbulent swirl flow encompasses a variety of applications, among the most widely used is the optimization of combustor firing, heat transfer intensity, and phase separators, among others.

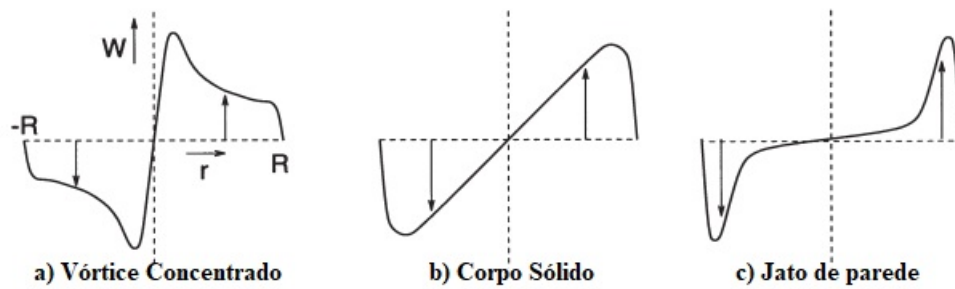
Swirling flow mostly has turbulent properties, for high Reynolds numbers between 10^4 and 10^5 . Because of this it becomes a highly complex flow that is difficult to predict and model experimentally and numerically. Well-founded experimental studies have been conducted to explore the characteristics of turbulent swirl flow (ALGIFRI; BHARDWAJ; RAO, 1988), (KITOH, 1991) and (STEENBERGEN, 1995).

The tangential velocity in flow with swirling through a pipe has a significant influence on the structure of the flow. The stream lines curved present in this type of flow are characterized mainly by the variation of tangential velocity and Reynolds' stresses (ALGIFRI; BHARDWAJ; RAO, 1988). There are three main regions: wall, annular, and core. The core region is characterized by a forced vortex motion that depends on the upstream conditions of the flow. Whereas in the annular region, there is high vorticity due to tangential velocity gradients and the effects are highly anisotropic, where the turbulent viscosity model does not work well. The tangential velocity being expressed as the sum of the free and forced vortex motion. At the wall there are wall effects due to shear forces. There are quite different turbulence structures in the core and outer regions. A swirling flow is affected by the curvature of the current lines as well as favorable and adverse pressure gradients. A Reynolds stress model that deals with anisotropic turbulence is a more promising way to model turbulent swirling flow compared to a turbulent viscosity model such as the $k - \epsilon$ (KITOH, 1991). The presence of a recirculation zone in the center of the vortex is a characteristic of swirling flows and develops in flows with a swirl number above a critical value, typically 0.6 (YAZDABADI; GRIFFITHS; SYRED, 1994).

Characteristic of turbulent swirling flow is the presence of axially concentrated vorticity near the wall and the center of the pipe. But the initially concentrated angular momentum is quickly dissipated since the circumferential shear rate produces high levels

of tangential shear stress $\langle vw \rangle$. There is the tangential velocity distribution radially with solid body rotation properties. In the core, the rotation rate, i.e., the local vorticity, remains constant along the flow development axis for approximately 20 times the diameter (STEENBERGEN, 1995). In the figure 8 there is a representation of these three regions.

Figure 8 – Swirl Region Classification (STEENBERGEN; VOSKAMP, 1998)



The turbulence properties are greatest in the core and with the decay of the swirl their magnitude reduces sharply, while changing subtly near the wall. The variation in tangential velocity can be approximated by a Rankine vortex. The three components of the mean velocity, turbulent intensities, and Reynolds stresses can be modeled with respect to Reynolds number, however, the radial component of the mean velocity has a small order of magnitude relative to the other two components (ALGIFRI; BHARDWAJ; RAO, 1988).

An important physical phenomenon present in turbulent flow is PVC (Processing Vortex Core) which is an instability present under certain operating conditions. They are present in cyclones operating on an industrial scale, due to high flow rates with high Reynolds numbers and presence of turbulence. Under these conditions, the central vortex is not aligned with the axis of symmetry of the cyclone, but presents a precession movement around it. This motion creates a high level of fluctuation in the flow field, especially in the central region of the cyclone, and also influences the separation of particles (HOEKSTRA, 2000). This is yet another characteristic phenomenon of turbulent swirl flow that depends on a good turbulence model prediction for a good numerical representation. Another common phenomenon found in turbulent flow is the Vortex Breakdown, is defined as stagnation of the axial velocity in the central axis (FRANCIA, 2015). This stagnation velocity is a result of the adverse pressure gradient generated by the centrifugal force at a given swirl intensity, as the swirl decays the centrifugal force decreases and forms a stagnation point. According to Lucca-Negro e O'Doherty (2014) the number of turns required to induce a recirculation and consequently the formation of the Vortex Breakdown is 0.6 and a critical Reynolds number of 1,000, i.e. for a strongly swirling flow.

2.5.1 Application of CFD in turbulent cyclone studies

The application of CFD to model and simulate cyclone flow began in the mid-1990s. Due to the limitation of data processors at that time, the first studies used the assumption of axisymmetry, i.e. two-dimensional modeling with isotropic turbulence models. However, the limitation of isotropic turbulence models, compared to experimental results of velocity profiles, would be related to the low resolution of the turbulent viscosity by the isotropic model.

Turbulence properties have a strong dependence on experimental studies, due to the complexity of numerical modeling and the need for data for validation of the proposed models. Thus, numerical studies are developed to contribute to scientific development in modeling turbulent swirling flows. Model prediction is one of the main tools to numerically represent the results found in experiments.

Due to its instability and nonlinearity of the inertial terms, turbulence requires thorough numerical modeling. An alternative to solving this problem is through partial differential equations, by discretizing the space and time coordinates. However, a comprehensive capture of the time and length scales of turbulent flow from direct resolution, the so-called DNS (Direct Numerical Simulation), becomes highly complex computationally applied to real engineering cases. With this, techniques such as LES (Large Eddy Simulation) which solves the Navier-Stokes equations for the larger scale swirls and models the smaller ones through isotropy and homogeneity. And the RANS technique (Reynolds Averaged Navier-Stokes) which statistically resolves the variables of the turbulent flow field by disassociating the level of discretization of the coordinates from the size of the turbulent scales makes it numerically possible to solve complex problems with less computational effort (WILCOX, 1998).

Thus the RANS technique is most studied in the literature for problems involving turbulent flow, especially the application of the k-e turbulence model, and its variations (BALI, 1998), (HOEKSTRA; DERKSEN; AKKER, 1999) and (JAWARNEH et al., 2009).

Bali (1998) obtained the numerical and experimental study of the flow with swirl using the k-e model due to the low swirl number. The isotropic turbulent viscosity was considered in the study due to the low tangential velocity at the inlet. The comparison between the experimental and numerical results showed good agreement.

Hoekstra, Derksen e Akker (1999) performed an experimental study of a swirling flow to validate the numerical results of different turbulence models (k-e standard, k-e RNG and RSM). The simulations performed from a two-dimensional model were done by the commercial software Fluent. In the study the RSM model showed the best result compared to the experimental one for axial velocity and tangential velocity, although it shows a discrepancy in the maximum tangential velocity values. It was possible to

notice a fluctuation of the tangential velocity compared to a time analysis, most likely due to the RANS modeling, overestimating the fluctuations in the free vortex region and underestimating the fluctuations in the forced vortex region.

[Jawarneh et al. \(2009\)](#) in a two-phase study between sand and oil from a numerical turbulent k-and RNG model compared with experimental data of the tangential velocity component and radial pressure profiles in order to describe the separation efficiency for high swirl number, where it obtained good agreement.

Other studies have been performed as an alternative way to isotropic modeling. Based on the k-e model ([MEIER; MORI, 1999](#)) developed a two-equation anisotropic model based on Prandtl's mixing length model. The application of the RSM model (Reynolds Stress Model) that has 6 equations was used by ([HOEKSTRA; DERKSEN; AKKER, 1999](#)) for cyclones. These alternatives showed improvements in modeling mainly the tangential velocity field and turbulence tensors.

One of the points discussed throughout the evolution of the application of CFD in cyclones is related to the influence of turbulence models in the fluctuations of the variables studied, especially the velocity. Fluctuations of high intensity can directly interfere in the process of particle separation, so the comparison between the average velocities obtained experimentally and simulation results using the RSM are essential. ([HOEKSTRA; DERKSEN; AKKER, 1999](#)) performed this comparison and showed that the Reynolds Stress model reproduced the anisotropy observed experimentally, but showed variations at high levels of velocity fluctuation in the center of the cyclone.

Some authors argue using the LES turbulence modeling technique for cyclone flows to capture all scales of turbulence. The essential difference between the RANS technique used in RSM modeling and the LES technique is that in the latter the swirls are resolved and a type of filter is used for smaller scales, whereas in the RANS model the turbulence is modeled. The RANS modeling may not be as robust as the LES technique, because the averaging process leads to loss of information regarding the structure of eddies, for example, but it requires significantly less computational cost with good results.

With advances in computer processing power and the development of turbulence models, current studies show the advantages of using the RSM turbulence model containing seven equations for solving Reynolds tensors ([NAJAFI et al., 2005](#)), ([MURPHY et al., 2007](#)) and ([KHODABANDEH et al., 2020](#)).

[Najafi et al. \(2005\)](#) In the experimental and numerical study the standard k-e, k-e RNG and RSM turbulence models were compared using the two-layer wall function to predict the swirl number decay. The vertical flow with swirl was applied by a honeycomb tube with swirl. In the comparison between the experimental and numerical data showed that the RSM model was more successful than the others used for comparison purposes.

Murphy et al. (2007) from a numerical study using two commercial software packages (Ansys Fluent® and CFX) analyzed the ability of each to predict the single-phase turbulent flow with swirl in an axial hydrocyclone using the RSM turbulence model. The numerically obtained results were compared with experimental data obtained by Dirkzwager (1996). Although the discrepancy in the axial and tangential velocity profiles of the numerical model compared to the experiment, especially near the center, the swirl decay obtained good agreement.

Khodabandeh et al. (2020) numerically studied turbulent flow with swirl applied to combustion by comparing RSM, standard k-e, and k-e RNG turbulence models with experimental data. Velocity profiles, energy dissipation rate, and exhaust pressure gradient were compared. The recirculation region was better estimated by the RSM model and consequently a better analysis of the swirl number, a prime variable for combustion optimization, could be obtained.

Based on the studies presented in the literature it is possible to conclude that the RSM model is the most appropriate for turbulent flows, due to its prediction for Reynolds tensors with 7 equations and more appropriate modeling for curved streamlines and anisotropic stresses (DIRKZWAGER, 1996), (DELFOS; DIRKZWAGER, 1998) and (SLOT, 2013).

2.6 Axial Hydrocyclone

A specific category of cyclones applied to separation is the axial inlet hydrocyclone, object of study of this dissertation. The hydrocyclones described in this topic have similar characteristics regarding the use of fixed vanes, constant diameter of the separation section and turbulent flow (LINDEN, 1949), (SWANBORN, 1988), (VERLAAN, 1991), (DIRKZWAGER, 1996), (DELFOS; DIRKZWAGER, 1998), (SLOT, 2013), (CAMPEN, 2014) and (KARIMPOORHEIDARI, 2019).

The application of axial inlet hydrocyclones for separation has been studied for over 70 years (STRAUSS, 1975). The goal is to design a rotational field inductor for separation that is more compact compared to tangential inlet cyclones.

One of the first studies in the literature applied to an axial inlet cyclone was developed by Linden (1949), where he conducted an experimental study of particulate matter collectors in an air stream through fixed propeller separation. It was pointed out by the author that one of the objects was to develop an axial inlet device, more compact than the traditional tangential inlet ones.

In oil and gas production the application of hydrocyclones for phase separation is widely used, with the objective of developing an axial inlet hydrocyclone, with lower

pressure drop, more compact and without the need for reverse flow, led [Swanborn \(1988\)](#) to carry out experimental and numerical studies with flows induced to swirl by static elements. In the analyses performed, promising results were obtained regarding the reduction of energy loss by friction and lower pressure drop. Continuing the studies of [Swanborn \(1988\)](#) and [\(VERLAAN, 1991\)](#) performed experimental and numerical studies by varying the characteristics of the static swirl-inducing element to the flow. Diameter and deflection angle of the fixed guides were varied. The author noted that the deflection angle of the flow is directly linked to the separation efficiency, where the tangential velocity component has a direct influence, presenting a higher efficiency for the largest adopted angle of 60.

[Dirkzwager \(1996\)](#) performed a single-phase turbulent experimental study of an axial inlet, fixed-vane cyclone separator. The separator geometry was developed for different flow deflection angles (45° , 63° and 72°) in order to observe the separation efficiency. The experimental data were obtained from the LCA technique. The main variables analyzed were the axial velocity profile, tangential velocity, the pressure field, and the swirl number. Continuing the study by [Dirkzwager \(1996\)](#) and [Delfos e Dirkzwager \(1998\)](#) performed single-phase (water) and two-phase (water-oil) experiments by changing some installation parameters, such as the horizontal operating position of the hydrocyclone, most common in industry. When the swirl is applied to the two-phase flow there is a phase separation due to the density difference. A reverse flow collection channel was added in the center of the hydrocyclone which resulted in a 50% percent increase in oil separation efficiency.

[Slot \(2013\)](#) based on the studies of [\(DIRKZWAGER, 1996\)](#) and [Delfos e Dirkzwager \(1998\)](#) focused on modeling and numerical simulations using CFD for single- and two-phase, turbulent, transient, 3D flow and with the presence of the static gyro generator in the pipe. A uniform inlet velocity of 2 m/s was defined upstream of the flow. Coalescence models for oil droplets, RANS turbulence model and the coupling between the oil and water equations in the two-phase eulerian flow model were incorporated. The results obtained are validated with the experimental results of [Campen \(2014\)](#) in a joint project that also counts with the collaboration of a study by [Krebs, Schroën e Boom \(2012\)](#) which focused on understanding and describing the various mechanisms of droplet coalescence in order to better understand how dispersion properties depend on oil properties. It was concluded by [Slot \(2013\)](#) that the results showed a large difference for the separation efficiency, the main parameter of the study, compared to the experimental results. This is mainly due to the numerical model not physically predicting the average droplet variation caused by coalescence. Although he proposes an improvement of the model, he points out that computational simulation is already costly. Regarding the turbulence model, he reiterates that the RANS model is the most appropriate for the application, but warns that the user should pay attention to the difference obtained for experimental results.

[Karimpoorheidari \(2019\)](#), from the analysis made by [Slot \(2013\)](#), studied the

characteristics of the flow with rotation in a circular session tube. Aiming at a reduction of computational cost, it simulated only the flow downstream of the swirl generator, taking as boundary conditions in its computational domain axial and tangential velocity profiles obtained by Slot (2013) from UDF (User Define Fuction). With the study of the flow with single-phase and turbulent swirl, it was noted that the formation of vortices in the flow is a function of the Reynolds number, and with this a critical number of swirl, called S , equal to 0.5, was determined, so that above this number there is the formation of reverse flow due to the formation of vortex breakdown.

2.7 Turbulent two-phase (liquid-gas) flow applied to separation

This topic presents numerical studies aimed at validated two-phase liquid-gas separation based on experimental data (ERDAL et al., 1997), (WANG et al., 2006), (LIU; BAI, 2017) and (YANG et al., 2020).

Erdal et al. (1997) performed a comparison between numerical and experimental approach of a tangential inlet and outlet cylindrical, for turbulent gas-liquid cyclonic separator. First a single-phase CFD study with the k-e turbulence model was applied. The two-phase study, performed from a gas phase dispersed in a liquid continuous phase, was developed by the mixing model. The axial velocity components, and decay of the tangential velocity were mainly analyzed. The axisymmetric modeling showed a good result compared to the three-dimensional modeling and the experimental data.

Wang et al. (2006) using the commercial Fluent software, they compared RSM turbulence models, Algebraic Stress Model e k-e, in which the RSM model showed better results compared to the experimental data. For two-phase modeling, the Lagrange model was used to represent the gas particles immersed in the liquid phase, where the interaction between the particles is disregarded. It was noted that for particles above the critical diameter of approximately $1 \cdot 10^{-5}$ m the particles have a tendency to remain stationary at the wall, harmful to the separation.

Liu e Bai (2017) presented a three-dimensional liquid-gas numerical study from the mixing model with different gas fractions, the turbulence model used was the k-e RNG. The radial velocity showed low influence on the separation compared to the axial and tangential velocities. The flow downstream of the separator showed regions of reverse flow, which was harmful to the separation. The swirl generator device showed a pressure drop close to half of the total static operating pressure. The separation efficiency is directly linked to the gas particle diameter, the separator geometry and the operating conditions.

Yang et al. (2020) obtained an experimental and numerical study, from the commercial package Ansys Fluent®, of a gas-liquid cyclonic separator from the DPM (Discrete Phase Model) modeling. The turbulence model used was the k-e RNG. It was noted

that higher swirl intensity is not necessarily better for separation efficiency. The particle diameter is directly linked to the coalescence of the mixture.

3 Numerical Modeling

3.1 Introduction

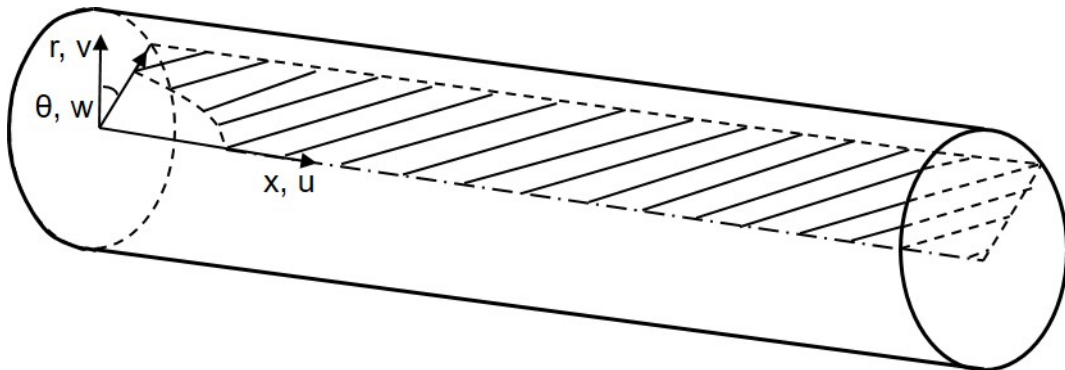
In this chapter, the mathematical modeling and the numerical method used in this study are presented.

Section 3.2 presents the mathematical formulation of laminar and turbulent regimes, from the equations of conservation of mass and momentum, containing the turbulence models. Also present in this section is the definition used to quantify the swirling flow. Finally, the equations governing the dynamics of a dispersed particle in a continuous fluid phase are expressed. In the next section 3.3, the numerical method used to solve the mathematical equations is described. Section 3.4 presents the computational domain together with the computational mesh, boundary conditions and convergence criteria.

3.2 Mathematical formulation

The swirling flow is modeled using the equations for conservation of mass and momentum. These equations are presented in a cylindrical coordinate system, as shown in figure 9. The velocity components u , v and w are the axial, radial and tangential velocities respectively and the variables x , r and θ are the axial, radial and tangential spatial coordinates respectively. The flow is considered axisymmetric (r, x) and periodic in the tangential direction (r, θ). The periodicity of the flow implies that there are no gradients in the direction θ . This approach is called a 3D axisymmetric computational domain with swirl. Furthermore, the fluid is considered Newtonian and the flow is isothermal and incompressible.

Figure 9 – Coordinate System (Source: Personal collection)



3.2.1 Laminar modelling

With the previously presented considerations, the equations of conservation of mass and momentum for a vertical flow in the steady state are described as (Bird, R. 2002):

- Equation of conservation of mass

$$\frac{1}{r} \frac{\partial}{\partial r}(\rho r v) + \frac{\partial}{\partial x}(\rho u) = 0 \quad (3.1)$$

- Radial momentum equation

$$\rho \left(v \frac{\partial v}{\partial r} + u \frac{\partial v}{\partial x} - \frac{w^2}{r} \right) = -\frac{\partial p}{\partial r} + \mu \left[\frac{\partial}{\partial r} \left(\frac{1}{r} \frac{\partial}{\partial r} (r v) \right) + \frac{\partial^2 v}{\partial x^2} \right] \quad (3.2)$$

- Tangential momentum equation

$$\rho \left(v \frac{\partial w}{\partial r} + u \frac{\partial w}{\partial x} + \frac{v w}{r} \right) = \mu \left[\frac{\partial}{\partial r} \left(\frac{1}{r} \frac{\partial}{\partial r} (r w) \right) + \frac{\partial^2 w}{\partial x^2} \right] \quad (3.3)$$

- Axial momentum equation

$$\rho \left(v \frac{\partial u}{\partial r} + u \frac{\partial u}{\partial x} \right) = -\frac{\partial p}{\partial x} + \mu \left[\frac{1}{r} \frac{\partial}{\partial r} \left(r \frac{\partial u}{\partial r} \right) + \frac{\partial^2 u}{\partial x^2} \right] + \rho g_x \quad (3.4)$$

The equations for conservation of mass and momentum can be written in the form of indicial notation. The advantage of indicial notation is that you can express the same physical meaning in a simplified form. In indicial notation, the previous four equations can be expressed as:

- Equation of conservation of mass

$$\frac{\partial u_i}{\partial x_i} = 0 \quad (3.5)$$

- Quantity of motion equation

$$\frac{\partial u_i}{\partial t} + u_j \frac{\partial u_i}{\partial x_j} = -\frac{1}{\rho} \frac{\partial p}{\partial x_i} + \frac{\partial \tau_{ij}}{\partial x_j} + g_i \quad (3.6)$$

where u_i and x_i are velocity and position respectively, t is time, p is pressure, and τ_{ij} is the stress tensor defined by:

$$\tau_{ij} = 2\pi\mu S_{ij} \quad (3.7)$$

where μ is the viscosity of the fluid and S_{ij} is the strain tensor, given by:

$$S_{ij} = \frac{1}{2} \left(\frac{\partial u_i}{\partial x_j} + \frac{\partial u_j}{\partial x_i} \right) \quad (3.8)$$

3.2.2 Turbulent modeling

Unlike laminar flow, which is steady, turbulent flow is chaotic, diffusive, time-dependent, three-dimensional with different time and length scales. Turbulence usually occurs at large Reynolds numbers and is a characteristic of the flow, not the fluid.

The most accepted turbulence theory is based on the "energy cascade" concept developed by Kolmogorov. According to this theory, turbulence is composed of different sized whirlpools, each possessing a certain amount of energy that depends on their size. The larger whirls break up by transferring their energy to smaller whirls in a chain process whereby the newly formed smaller whirls undergo similar breaking processes and transfer their energy to even smaller whirls. This breaking process continues until the smallest possible tourbillon size is reached. The smallest swirls are of scales at which molecular viscosity is very effective in dissipating the turbulent kinetic energy as heat.

The smallest swirls are characterized by the Kolmogorov length (η) and time (t) scale:

$$\eta = \left(\frac{\nu^3}{\varepsilon} \right)^{\frac{1}{4}} \quad (3.9)$$

$$t = \left(\frac{\nu}{\varepsilon} \right)^{\frac{1}{2}} \quad (3.10)$$

where η is kinematic viscosity and ε is the average rate of kinetic energy dissipation. The size of the largest swirls is defined as being proportional to the size of the geometry involved.

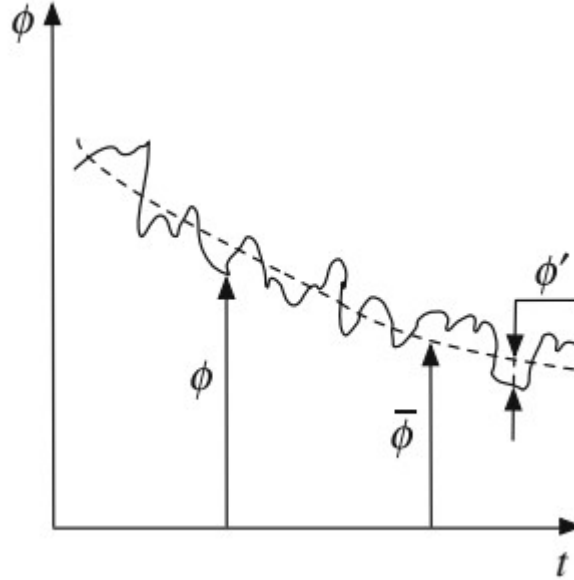
Based on the energy cascade concept, a direct numerical solution of the Navier-Stokes equation for turbulent flows requires the use of a very small time interval, bounded by a Courant number below 1 and a fine mesh ($\Delta x < \eta$), resulting in a large number of grid points (proportional to Re^3) to solve the full spectrum of temporal and spatial turbulent scales involved. This computationally demanding approach, denoted in the literature as Direct Numerical Simulation (DNS). Due to its prohibitive computational cost, the DNS approach cannot currently be employed to solve industrial problems. Future advances in computing technology may change the situation in favor of DNS.

An alternative, less computationally expensive, simulation is LES (Large Eddy Simulation). In it, large scales are solved directly while small scales are modeled. The key

concept of LES is to filter the Navier-Stokes equation to determine which scales to keep and which to discard. With recent advances in computer technology, the use of LES to solve industrial problems has gained good acceptance.

However, currently the most popular approach for dealing with turbulent flow problems is the one based on solving the Reynolds Averaged Equations (RANS), where the time-based statistical average (time-averaged) is used. The key concept is to decompose the flow variables into a time-averaged value component and a fluctuating component (figure 10), substituting in the original equations and averaging the obtained equations over time. Although the name refers to the Navier-Stokes equation, the decomposition is applied to all governing equations.

Figure 10 – Variation of ϕ with time (Source:)



3.2.3 Reynolds Average

Consider that ϕ represents at time t and position x the instantaneous value of any of the flow variables involved. Then, as shown in figure 10, it is decomposed into a mean value component $\bar{\phi}(x, t)$ and a fluctuating component $\phi'(x, t)$ such that:

$$\phi(x, t) = \bar{\phi}(x, t) + \phi'(x, t) \quad (3.11)$$

where the mean value $\bar{\phi}$ is calculated as:

$$\bar{\phi}(x) = \frac{1}{T} \int_t^{t+T} \phi(x, t) dt \quad (3.12)$$

Substituting the instantaneous variables into equations 3.5 and 3.6, and taking the average of the entire equation, gives the RANS equations (equations 3.13 and 3.14) (WILCOX,1998).

$$\frac{\partial \bar{U}_i}{\partial x_i} = 0 \quad (3.13)$$

$$\frac{\partial \bar{U}_i}{\partial t} + \bar{U}_j \frac{\partial \bar{U}_i}{\partial x_j} = -\frac{1}{\rho} \frac{\partial \bar{p}}{\partial x_i} + \frac{\partial}{\partial x_i} (\tau_{ij} - \bar{u}'_i \bar{u}'_j) + \bar{g}_i \quad (3.14)$$

The term $-\bar{u}'_i \bar{u}'_j$ is known as Reynolds stress tensor (R_{ij}) Reynolds tensions are components of a second-order, symmetric tensor can be written as:

$$R_{ij} = -\bar{u}'_i \bar{u}'_j = -\rho \begin{bmatrix} \bar{u}'\bar{u}' & \bar{u}'\bar{v}' & \bar{u}'\bar{w}' \\ \bar{v}'\bar{u}' & \bar{v}'\bar{v}' & \bar{v}'\bar{w}' \\ \bar{w}'\bar{u}' & \bar{w}'\bar{v}' & \bar{w}'\bar{w}' \end{bmatrix} \quad (3.15)$$

Note that the terms of the equation of (R_{ij}) are unknown and thus the system of equations cannot be solved, a priori. Solving the system of equations requires constitutive (or closure) equations. The process of calculating Reynolds stresses is denoted in the literature as turbulence modeling. Trying to develop such equations using the original conservation equations results in additional unknowns (such as triple products of the fluctuating components) further complicating the problem. The Reynolds stress tensor comes from the nonlinear convection term of momentum and temperature, confirming that turbulence itself is the effect of a nonlinear phenomenon that is highly sensitive to any perturbation. To overcome this problem, any turbulence model has to close the system of equations by expressing the fluctuating nonlinear stress components only in terms of the mean components, as described below.

As it is, the system is not closed and needs closure equations to be solved numerically, with given initial and boundary conditions, to obtain the mean field (\bar{U}_i and \bar{P}), the Reynolds stress tensor must be expressed from auxiliary equations.

The closure equations are obtained from the modeling of the turbulent viscosity. The Boussinesq hypothesis, created in 1877, adopts the assumption of isotropic viscosity, i.e. the mean turbulent quantities have the same value in all directions. In this approach, the stress tensor is proportional to the strain rate (equation 3.16), which is the basis modeling for several isotropic turbulence models.

$$R_{ij} = -\bar{u}'_i \bar{u}'_j = 2\mu_\tau S_{ij} - \frac{2}{3}k\delta_{ij} \quad (3.16)$$

where μ_τ represents the turbulent viscosity, δ_{ij} is the Kronecker delta and k (equation 3.17) the turbulent kinetic energy.

$$k = \frac{1}{2} \bar{u'_i u'_i} \quad (3.17)$$

Finally, substituting the definition of the Boussinesq hypothesis (equation 3.18) into the RANS equation gives the following expression:

$$\frac{\partial \bar{U}_i}{\partial t} + \bar{U}_j \frac{\partial \bar{U}_i}{\partial x_j} = -\frac{1}{\rho} \frac{\partial}{\partial x_i} \left(\bar{P} + \frac{2}{3} \rho k \right) + \frac{\partial}{\partial x_i} (2\mu_{eff} S_{ij}) + \bar{g}_i \quad (3.18)$$

In which, $\mu_{eff}(x, t) = \mu_\tau(x, t) + \mu$, i.e., the effective viscosity is the sum of the viscosity of the working fluid plus the viscosity produced by the turbulent flow. Thus, the definition of the turbulent viscosity is sufficient for the closure of the system, a procedure that distinguishes the turbulence models.

Several turbulence models based on the Boussinesq hypothesis have been developed to express turbulent viscosity, and none of them are universally applicable to all flow conditions. The models are grouped into four categories:

Zero Equation Models: uses an algebraic equation to calculate the turbulent viscosity without the need to solve any differential equation. This category includes the Mixture Length models of Prandtl (1925), Van Driest (1956), Spalding (1961), and Smith and Cabeci (1967).

One-Equation Models: requires solving only one differential transport equation to calculate the turbulent viscosity of the whirlpool. This category includes the models of Prandtl (1945), Baldwin and Barth (1990), and Sparlat and Allmaras (1992).

Two Equation Models: Two equation turbulence models are the most popular in terms of use in industrial simulation applications and require the solution of two transport equations to calculate the turbulent viscosity. In this category one can mention the $k - \varepsilon$ model initially proposed by Launder and Spalding (1972) and with different variations (Jones and Lauder (1972), Launder and Sharma (1974), Launder et al (1977), Lam and Bremhorst (1981), Speziale (1987) and Jakhot and Orszag (1986)), the $k - \varepsilon$ model initially proposed by Kolmogorov (1942) and with different variations (Wilcox (1988) and Menter (1994)).

Second-Order Closure Models: Second-order closure models are the most computationally expensive because separate transport equations are solved for the individual turbulent flows. In this category one can mention the RSM model (Launder et al., 1975; Gibson and Launder, 1978 and Launder, 1989).

Since turbulent flow with swirl is anisotropic, the RSM model is recommended. The

initialization of the calculation process is performed with the isotropic two-equation $k - \varepsilon$ model. This procedure is a common practice and recommended by Ansys as it contributes to stability during the first interactions where gradients are high. The two models used will be presented below, all the steps for obtaining the equations can be found in Wilcox (2006).

3.2.4 K- ε Model

The $k - \varepsilon$ model is one of the isotropic turbulent viscosity models, present in the literature, which was used in this study. It is also known as a two-equation model, because to solve the model, two transport equations are solved (one for k and another for ε), in addition to the equations of conservation of mass and momentum. The turbulent viscosity of this model is defined as:

$$\mu_\tau = \frac{C_\mu k^2}{\varepsilon} \quad (3.19)$$

where C_μ is one of the model constants, k is the turbulent kinetic energy, calculated by equation 3.17, and ε is the turbulent energy dissipation rate, calculated by equation 3.19.

$$\frac{\partial k}{\partial t} + \bar{U}_j \frac{\partial k}{\partial x_j} = R_{ij} \frac{\partial \bar{U}_i}{\partial x_j} - \varepsilon + \frac{\partial}{\partial x_j} \left[\left(\mu + \frac{\mu_\tau}{\sigma_k} \right) \frac{\partial k}{\partial x_j} \right] \quad (3.20)$$

$$\frac{\partial \varepsilon}{\partial t} + \bar{U}_j \frac{\partial \varepsilon}{\partial x_j} = C_{\varepsilon 1} R_{ij} \frac{\partial \bar{U}_i}{\partial x_j} - C_{\varepsilon 2} \frac{\varepsilon^2}{k} + \frac{\partial}{\partial x_j} \left[\left(\mu + \frac{\mu_\tau}{\sigma_\varepsilon} \right) \frac{\partial \varepsilon}{\partial x_j} \right] \quad (3.21)$$

Table 1 shows the model coefficients obtained experimentally.

Table 1 – Model closure constants k- ε

C_μ	σ_k	$C_{\varepsilon 1}$	$C_{\varepsilon 2}$	σ_ε
0.09	1.0	1.44	1.92	1.3

This model is widely used in CFD application, although it is a simple model. It is stable due to the stability promoted in the mean flow by the second order gradients. For being isotropic, it has a good accuracy of the normal stresses, but has difficulties in computing the effects of curvature and recirculations, i.e., as much as it has a good accuracy for simple flows, it is inaccurate for complex flows that have high vorticity as is the case of flows with high swirl, the focus of this study (POPE, 2000).

3.2.5 Reynolds Stress Model

Although it is an averaging model, just like $k - \varepsilon$, its main difference is in the modeling of the turbulent stress. The Reynolds Stress model includes anisotropic effects of

turbulence, unlike the Boussinesq hypothesis. With this, it becomes superior to isotropic models when used to simulate flows that exhibit rotation and curved streamlines. The accuracy is limited by the closure assumptions, obtained by semi-empirical methods, to model various terms in the transport equations. Equation 3.22 expresses the stress tensor transport equation (SPEZIALE, SARKAR AND GATSKI,1991) and were obtained from the study done by Slot (2013).

$$\frac{\partial R_{ij}}{\partial t} + \bar{U}_k \frac{\partial R_{ij}}{\partial x_k} = P_{ij} + \Pi_{ij} - \varepsilon_{ij} + \frac{\partial}{\partial x_k} \left[\mu \frac{\partial R_{ij}}{\partial x_k} \right] \quad (3.22)$$

where P_{ij} is the stress production, Π_{ij} the viscous dissipation, and ε_{ij} the stress due to pressure.

To transform the transport equation for Reynolds stresses into a closed system for mean values, the subscript terms in equation 3.22 are represented as empirical functions of the mean flow velocities and Reynolds stresses. The first model for Reynolds stresses was presented by Rotta 1951, used as the basis for other variations that came later. In this study the modeling proposed by Speziale, Sarkar and Gatski (1991) will be used. For incompressible and isothermal flow, the equation is expressed by:

$$\frac{\partial R_{ij}}{\partial t} + \bar{U}_k \frac{\partial R_{ij}}{\partial x_k} + \frac{\partial T_{ijk}}{\partial x_k} = P_{ij} + R_{ij} - \varepsilon_{ij} \quad (3.23)$$

P_{ij} is the production tensor that provides the Reynolds stresses generated by the gradients of the mean velocity of the flow. This procedure transfers the kinetic energy from the mean velocity field to the buoyancy velocity field. This tensor is given by:

$$P_{ij} = - \left(\bar{u}'_i \bar{u}'_k \right) \frac{\partial \bar{U}_j}{\partial x_k} - \left(\bar{u}'_j \bar{u}'_k \right) \frac{\partial \bar{U}_i}{\partial x_k} \quad (3.24)$$

T_{ijk} is a diffusive gradient combination, given by:

$$T_{ijk} = - \left(\mu + \frac{2}{3} C_s \frac{k^2}{\varepsilon} \right) \frac{\partial \bar{U}_i}{\partial x_k} \quad (3.25)$$

where C_s is a constant.

The pressure deformation tensor R_{ij} is crucial to the model and has been a subject of extensive research. For the SSG model it is given by equation 3.26, the constants are expressed in table 2.

$$R_{ij} = -C_{r1} \frac{P}{\rho} a_{ij} + C_{r2} k S_{ij} - C_{r3} k S_{ij} \sqrt{a_{lm} a_{lm}} + C_{r4} k \left(a_{ik} S_{jk} + a_{jk} S_{ik} - \frac{2}{3} a_{kl} S_{kl} \delta_{ij} \right) + C_{r5} k (a_{ik} \Omega_{jk} + a_{jk} \Omega_{ik}) \quad (3.26)$$

Table 2 – Model closure SSG

C_{r1}	C_{r2}	C_{r3}	C_{r4}	C_{r5}
0.9	0.8	0.65	0.625	0.2

where P is the turbulent kinetic energy output, given by:

$$P = - \left(\bar{u}_k' \bar{u}_l' \right) \frac{\partial \bar{U}_k}{\partial x_l} \quad (3.27)$$

and Ω_{ij} is the average vorticity tensor, expressed by:

$$\Omega_{ij} = \frac{1}{2} \left(\frac{\partial \bar{u}_i}{\partial x_j} - \frac{\partial \bar{u}_j}{\partial x_i} \right) \quad (3.28)$$

the dissipation tensor is modeled as:

$$\varepsilon_{ij} = \frac{2}{3} \delta_{ij} \varepsilon \quad (3.29)$$

Finally, ε is the rate of dissipation of turbulent kinetic energy, given by equation 3.30, whose constants are in table 3.

$$\varepsilon_{ij} = \frac{2}{3} \delta_{ij} \varepsilon \quad (3.30)$$

Table 3 – Model closure rate of dissipation

C_{RS}	$C_{\varepsilon 1}$	$C_{\varepsilon 2}$
0.066	1.45	1.83

3.2.6 Wall function

Near the wall are located high velocity gradients due to the properties related to the viscous boundary layer. This region is divided into three main parts, they are: the viscous underlayer that is close to the solid surface and is where the viscosity effects predominate. Above this is the transition zone to the third region, the turbulent sub-layer, which is bounded by the boundary layer. To accurately predict the flow fields, it is necessary to refine the computational mesh close to the wall. Additional damping functions are also required in the turbulence models to ensure their validity in the viscous sublayer. However, the former procedure increases the computational cost of simulation and the latter increases the complexity of the model. Both problems can be solved using the wall function, expressed by equation 3.31 (POPE, 2000).

$$\bar{u}_1 = u_\tau \left[\frac{1}{k} \ln(y^+) + B \right] \quad (3.31)$$

where \bar{u}_1 is the velocity at the surface, k is known as the Von Kármán constant whose value is 0.41, B is the integration constant that incorporates the roughness of the material surface, for smooth surfaces has a value of 0.5. These constants are obtained experimentally (POPE, 2000). u_τ is the friction velocity, expressed by:

$$u_\tau = \frac{\sqrt{\tau_w}}{\rho} \quad (3.32)$$

The wall shear stress is expressed by: τ_w . The dimensionless number representing the distance from the wall, as:

$$y^+ = \frac{yu_\tau}{\nu} \quad (3.33)$$

where y is the normal distance to the wall. However, the equation 3.33 becomes singular when the wall shear stress approaches zero. Hence, the friction velocity u_τ in natural logarithm is replaced by another expression for the velocity scale, the nominal friction velocity, given by:

$$u_\tau^* = C^{\frac{1}{4}} k^{\frac{1}{2}} \quad (3.34)$$

Thus, even when the wall shear stress is zero, u_τ^* will be non-zero. The derivation of the nominal friction velocity is based on two-equation turbulence modeling, as is the $k - \varepsilon$ model, for which the wall function approach was initially developed. Given the proper modeling, the equations are satisfied by:

$$\varepsilon = \frac{C_\mu^{\frac{3}{4}} k^{\frac{3}{4}}}{ky} \quad (3.35)$$

In which the constants are the same as in table 1. The transition from the log layer to the viscous sublayer is often considered to be the point where the linear velocity profile of the viscous sublayer and the logarithmic velocity profile of the log layer intersect, i.e., at $y^+ = 11.06$. Therefore, it is recommended that y^+ stays below this value (Slot, 2010). Wall functions assume that the velocity profile follows the logarithmic law, equation 3.33, so these functions fail if the velocity profile deviates from this. Measurements by Kitoh (1991) for a flow with moderate swirl, agree well with the log-law for $y^+ < 100$. Furthermore, Murphy (2007) concludes that in general his numerical simulations predicted the near-wall behavior very well and thus confirming the applicability of the wall functions even for strongly agitated flows.

3.2.7 Swirl number

To quantify the intensity of the swirl of the flow inside the tube, a dimensionless number is used that represents the ratio between the angular momentum flow and the axial momentum flow. In the present study, the definition given by Kitoh (1991) was adopted.

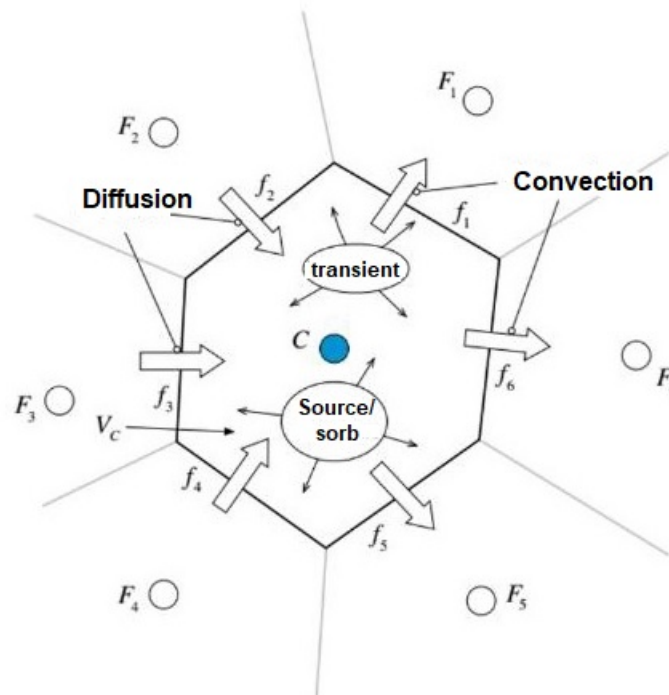
$$S = \frac{2 \int_0^R uwr^2 dr}{R^3 U_{avg}^2} \quad (3.36)$$

where R is the radius of the tube and U_{avg} the average axial velocity.

3.3 Numerical method

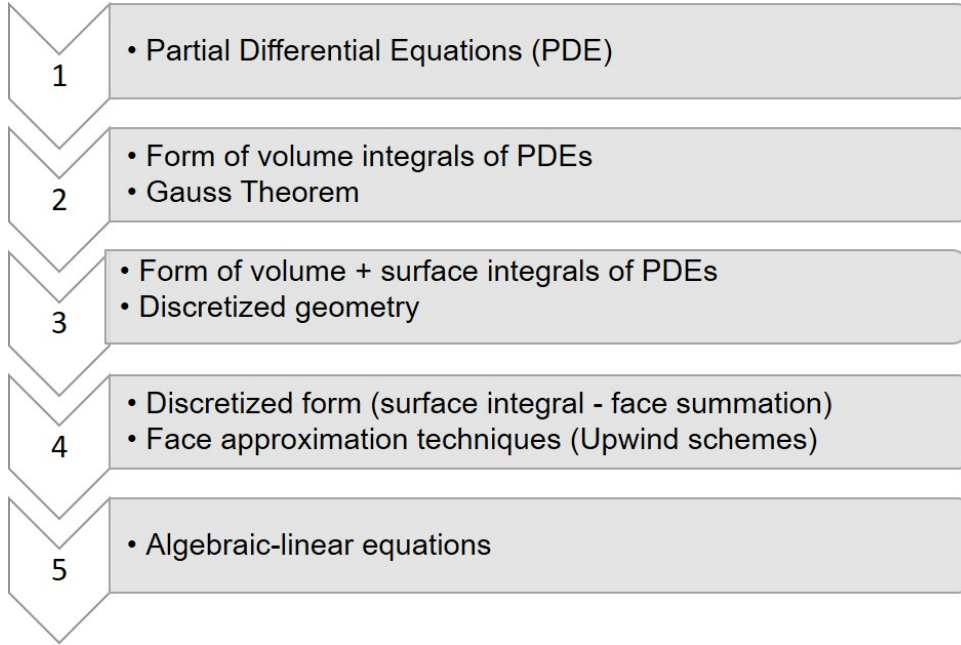
The numerical resolution of partial differential equations are solved by discretizing the time and space coordinates. In this study we used the finite volume method to discretize the transport equations from the integral of the conservation equation. Because it has a clear physical interpretation, it is a method widely used in engineering. The computational domain is divided into a finite number of control volumes where the set of equations is applied to the centroid of each element, called computational node, where the variables are calculated point by point. Figure 11 represents diffusion and convection in a control volume.

Figure 11 – Convective and diffusive flow in the control volume (Source: Moukalled et al. (2016))



The values of the surfaces of control volumes are obtained by interpolating as a function of node values, and methods are used for this application. For control volumes that are adjacent to domain boundaries the equations incorporate boundary conditions. The resulting system of linear algebraic equations is solved to obtain the distribution of the property in question at the nodal points. Figure 12 illustrates how the numerical method is solved.

Figure 12 – Numerical method (Source: Anderson, J. D. (1995))



3.3.1 Discretization of the governing equations

The equations governing the flow are integrated into each control volume. The derivatives of the diffusive and convective terms are approximated by interpolation functions. Consequently, a set of algebraic equations to be solved is obtained. There are different interpolation functions that are associated with the discretization order. For high-order functions the results obtained are more accurate than for low-order functions. However, the higher the order used, the higher the associated computational cost, requiring higher processing requirements and simulation time. The convection-diffusion equation for a general property in the control volume is expressed by (Versteeg, Malalasekera, 2007):

$$\int_A \mathbf{n} \cdot (\rho \phi \mathbf{u}) dA = \int_A \mathbf{n} \cdot (\Gamma \nabla \phi) dA + \int_{V_c} S_\phi dV \quad (3.37)$$

The term on the left side of the equality gives the convective flow, on the right side the diffusive flow is added to the source term of the flow. The main problem in discretizing the convective terms is the calculation of the value of the property carried on the faces of the control volume and its convective flow across these boundaries. For this study, we

adopted the upwind differentiation scheme that takes into account the direction of flow, the convected value of the property carried on the face of the control volume is considered equal to the value at the upstream node. The first-order upwind method increases the numerical diffusion, error due to the truncation of the discretization of the governing equations, which reduces the accuracy of the solution or presents physically inconsistent result. With this, the second-order upwind method that uses two upstream neighboring nodes to estimate the value at the cell face was used. Even with a higher computational effort, upwind interpolation has a higher numerical stability (Versteeg, Malalasekera, 2007).

For pressure interpolation, the PRESTO! (Pressure Staggering Option) method, which is suitable for simulations with rotation (Kulkarni, Ranade, Rajeev and Koganti (2008), Shukla, Shukla and Ghosh (2011)). The method performs discretization on the face of each element by imposing a pressure gradient on the boundaries, which increases the stability of the solution.

3.3.2 Temporal Discretization

In transient simulations the time variable is added to the equations and they are solved at each time step. The process involves integrating all the terms in the differential equations over a time interval. In this study, transient simulations are used to study turbulent swirling flow.

There are two main methods of time discretization: implicit and explicit. The explicit method is used when there is a density-based solution, in this method the time interval is restricted to the stability limit of the solution, i.e., to be accurate and stable all elements of the computational domain must use the same time interval, so the time step used must be associated with the smallest mesh element. The implicit method is used for incompressible flows because it is pressure-based, it is solved iteratively for each time step that the equation is discretized before proceeding to the next physical time step. The advantage of the implicit method is that it is unconditionally stable with respect to the size of the time interval. However, due to the iterative procedure it requires higher computational processing cost. Equation 3.38 mathematically represents the first-order implicit method used in this study, in which Δt represents the time interval.

$$F(\phi_{n+1}) = \frac{\phi_{n+1} - \phi_n}{\Delta t} \quad (3.38)$$

One of the challenges is to choose the correct time-step value for solving the transient simulation relating computational time and accuracy. The CFL (Courant - Friedrichs - Lewy) number is used to estimate the approximate time step for stability of the solutions. It relates the average flow velocity \bar{u} , the maximum time step Δt , and the dimension of

the smallest mesh element in the flow direction Δx . It is represented mathematically as:

$$C_o = \frac{\bar{u}\Delta t}{\Delta x} \quad (3.39)$$

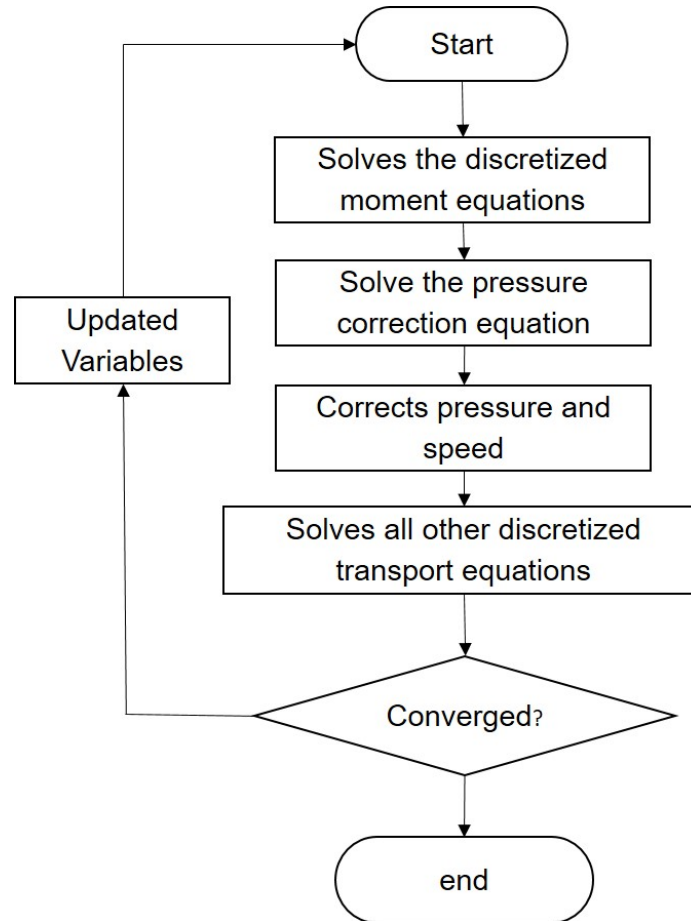
For the explicit method, a Courant number less than or equal to 1 is indicated, which physically represents as the residence time of the fluid in each mesh cell, where with a value equal to 1, it is guaranteed that a fluid element travels only one mesh cell at each time step. However, by using the shortest length of a mesh element, C_o can be overestimated for the implicit method and in a mesh of heterogeneous sizes. Thus, it is necessary to evaluate the stability of the solution, and to adopt C_o that does not exceed a value equal to 100 as a reference. Besides the C_o , the definition of the total simulation time is important, and can be estimated from the volume of the computational domain and the average velocity at the inlet of the flow. The flow development varies in each case, however, it is recommended as total simulation time, at least three times the characteristic time, where once is for flow development and twice for obtaining the temporal average of the variables (AGUIRRE; DAMIAN, 2008). However, this total simulation time can be impeditive in some complex simulations, as in turbulent flows for example, where several equations are solved at each time step, which demands a high computational cost for large domains. An alternative is to monitor the variables of interest to detect the stability of the solution once the flow has developed.

3.3.3 Coupling pressure and velocity

One of the challenges of numerical simulation for flow is to obtain a mathematical expression for the calculation of pressure in order to solve the whole system of equations of the numerical method. Taking into account the strong coupling between pressure and velocity, a pressure-based algorithm was developed to solve this problem, called the projection method (CHORIN, 1968). In this method the pressure equation is derived from the continuity and momentum equations so that the velocity field, corrected for pressure, satisfies continuity. Since the governing equations are nonlinear and coupled together, the solution process involves iterations in which the entire set of governing equations is solved repeatedly until the solution converges. There are two pressure-based algorithms: segregated and coupled. In segregated solving the governing equations are solved sequentially, that is, segregated from each other. Since the governing equations are nonlinear and coupled, the solution loop must be performed iteratively to obtain a convergent numerical solution. Two segregated algorithms are the most widespread in the literature: SIMPLE (Semi-Implicit Method for Pressure Linked Equations) and SIMPLEC (Semi-Implicit Method for Pressure Linked Equations-Consistent). The coupled method, on the other hand, as the name indicates, solves a coupled system of equations that comprises the pressure-based momentum and continuity equations. Since the equations are solved in

a coupled fashion, the convergence rate of the solution improves significantly compared to the segregated algorithm. However, memory processing increases by up to two times compared to the segregated algorithm, since the system of all equations must be stored in memory when solving the velocity and pressure fields (ANSYS, 2018). The algorithm used in this work is Simple and is depicted in figure 14.

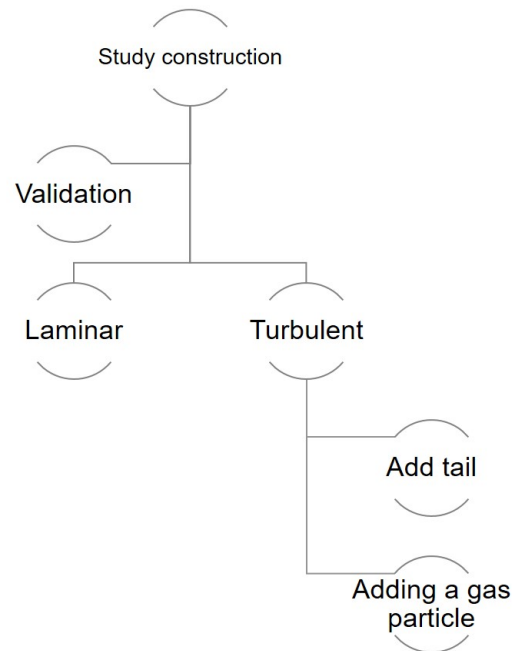
Figure 13 – Pressure-Based solution method (Source: Adapted from Ansys (2018))



3.3.4 Study methodology

From the mathematical modeling and the numerical method presented, a sequence of steps was developed to solve the physical phenomena that were proposed by this study. It began with numerical validation, which is essential to ensure that the methodology adopted, based on the literature, represents a physically real flow. Two distinct cases were validated, one for laminar flow and another for turbulent flow. For laminar flow the numerical study performed by Ayinde (2010) was selected. For the turbulent modeling, an experimental study by Diekzwager (1996) was used. With the validated numerical model, studies of the effect of the tail in the flow and the addition of a dispersed gas particle in the continuous liquid phase were performed. Figure 14 illustrates the construction of this study.

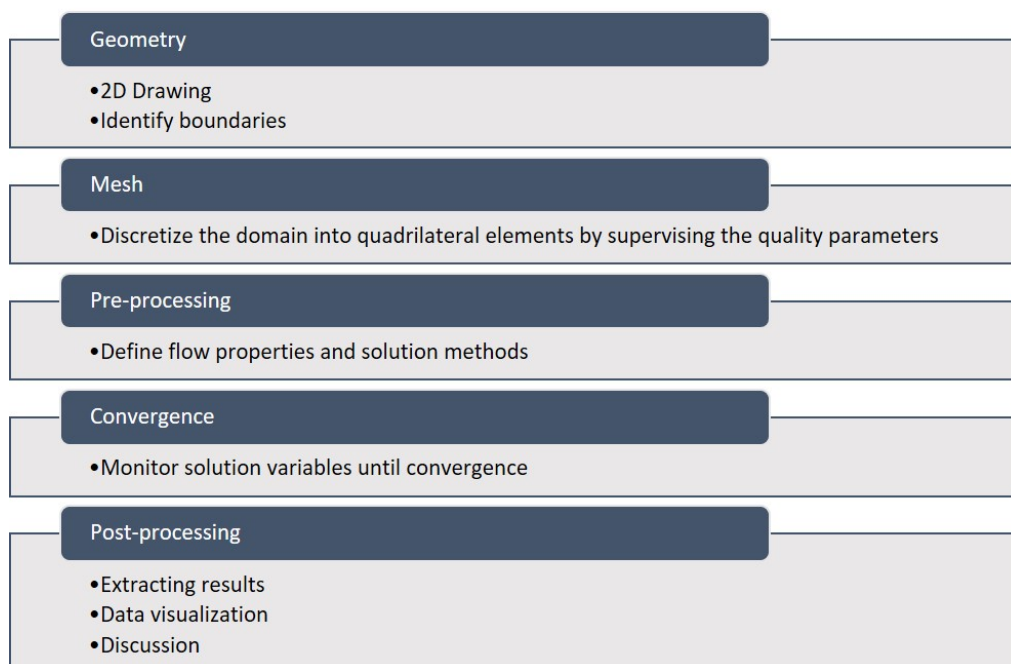
Figure 14 – Study construction(Source:Personal collection)



3.3.5 Steps

For all the steps presented above, the commercial package Ansys® Fluent was used. Figure 15 illustrates the steps used to obtain the flow results, from geometry creation to post-processing.

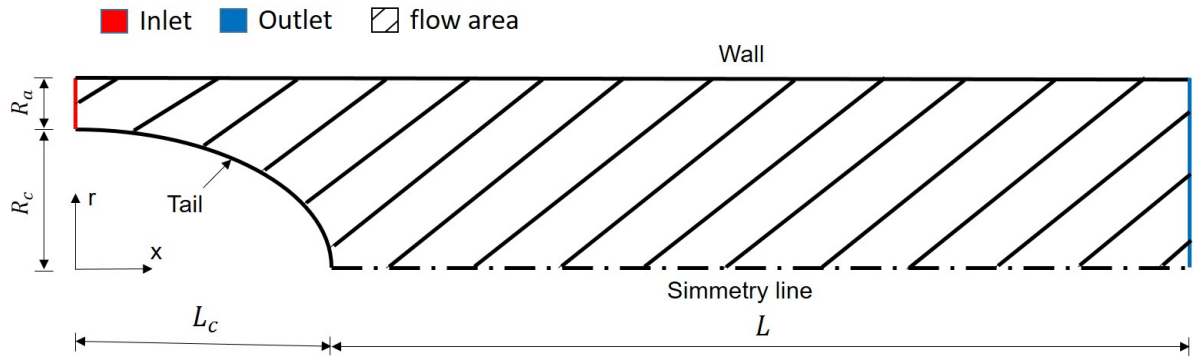
Figure 15 – Flow solution steps (Source: Personal collection)



3.4 Computational domain

The computational domain is the region where there is the discretization of the computational mesh for application of the finite volume method. Figure 17 illustrates the computational domain of the separation section of an axial hydrocyclone, formed by a circular axisymmetric tube divided into two regions: the annular tail region and the constant section region after the tail. The flow develops in the positive x-axis direction of the (x, r) plane. The variables that form the geometry of the domain are: R_a which represents the annular radius, R_c which is the cone radius, L_c is the length of the cone and L represents the length of the constant radius section. The total radius of the domain is the sum of R_a and R_c and has value 25 mm, Whereas the total length which is the sum of L_c and L with value 3,375 mm.

Figure 16 – Computational domain (Source: Personal collection)



3.4.1 Computational mesh

The flow of the conserved properties can be directly affected by the arrangement and shape of the control volumes. It affects the accuracy of the solution, the numerical convergence rate, and the computational time. Thus, the generation of a suitable mesh becomes of paramount importance in the solution of the finite volume method. Some parameters are used to ensure the quality of the mesh, where they are associated with the geometric shape of each control volume and the connectivity with its neighbors. In this study took into consideration three mesh parameters (ANSYS THEORY 2013), they are:

- **Aspect ratio:** ratio between the largest and smallest edge of the element, in the ideal case a value close to 1 is desired. For high values it can lead to errors in the numerical approximation of the flows at the face.
- **Asymmetry:** represents the offset of the vector connecting the center of the neighboring volumes and the center of the face. High asymmetry values can degrade

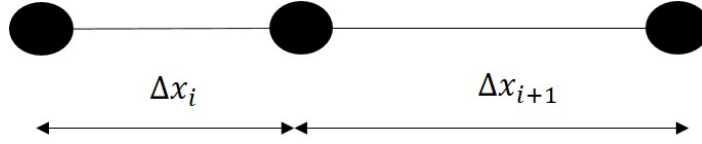
the numerical solution. The asymmetry number is obtained from the following formulation:

$$S_k = \max \left[\frac{90 - \alpha_{\max}}{90} \right] \quad (3.40)$$

where α_{\max} represents the largest angle on the faces of the volume. The value of asymmetry is between 0 and 1, with 0 being the best possible value and 1 being the worst value. It is recommended to use $S_k < 0.85$.

- **Smoothing:** This metric is related to the transition in the size of adjacent volumes in the mesh. This transition should be smooth to avoid truncation errors in the numerical approximations for calculating flows over the volume surfaces. It is recommended to use variations with a ratio of less than 20% between volumes, according to equation 3.41. Figure 17 represents the arrangement between the nodes of the control volumes.

Figure 17 – Smoothing between control volumes (Source: Personal collection)

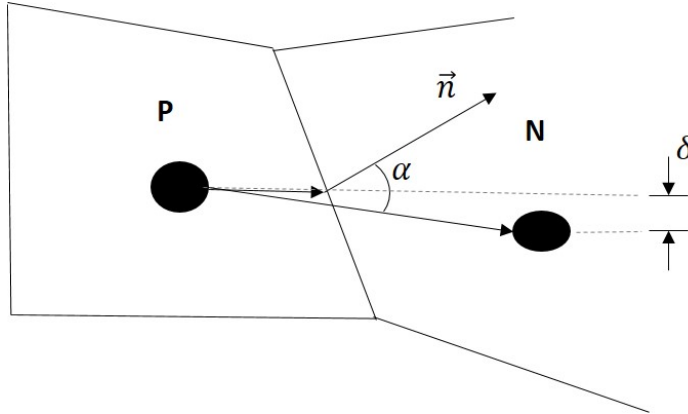


thus:

$$\frac{\Delta x_{i+1}}{\Delta x_i} \leq 1.2 \quad (3.41)$$

- **Orthogonality:** refers to the deviation of the angle between the vector connecting the center of adjacent volumes and the vector normal to the surface between them (δ). Figure 18 illustrates the parameter.

Figure 18 – Orthogonality (Source: Personal collection)



The occurrence of non-orthogonality affects the accuracy of the numerical approximation of flows, especially the discretization of the gradient operator. Mesh with high

orthogonality may suffer from numerical diffusion errors in solving the problem. Thus, it is desired the smallest possible value of orthogonality.

In view of the meshing needs, aiming to accurately capture the flows and lower computational cost, all meshes were modeled with quadrilateral elements using the commercial tool Ansys Meshing. This type of modeling is also recommended for better boundary layer accuracy. The refinement is an important and necessary technique to accurately measure the phenomena in specific regions of the computational domain. Thus, the meshes in the radial direction near the wall were refined as a function of y^+ , as shown in figure 19. However, getting the dimension of the first element adjacent to the wall right is critical, because of the need for it to ideally reside within the log-law region. The viscous layer has an intersection with the log-layer at $y^+ = 11$, which is accepted as the closest distance to the adjacent wall in many meshes. It is therefore recommended to use values of y^+ in the range of: $30 < y^+ < 100$ (SLOT (2013) and KARIMPOORHEIDARI (2019)). The meshes were defined so that the boundary layer resulted in a suitable dimensionless height (defined by equation 3.33).

Figure 19 – Boundary layer (Source: Personal collection)

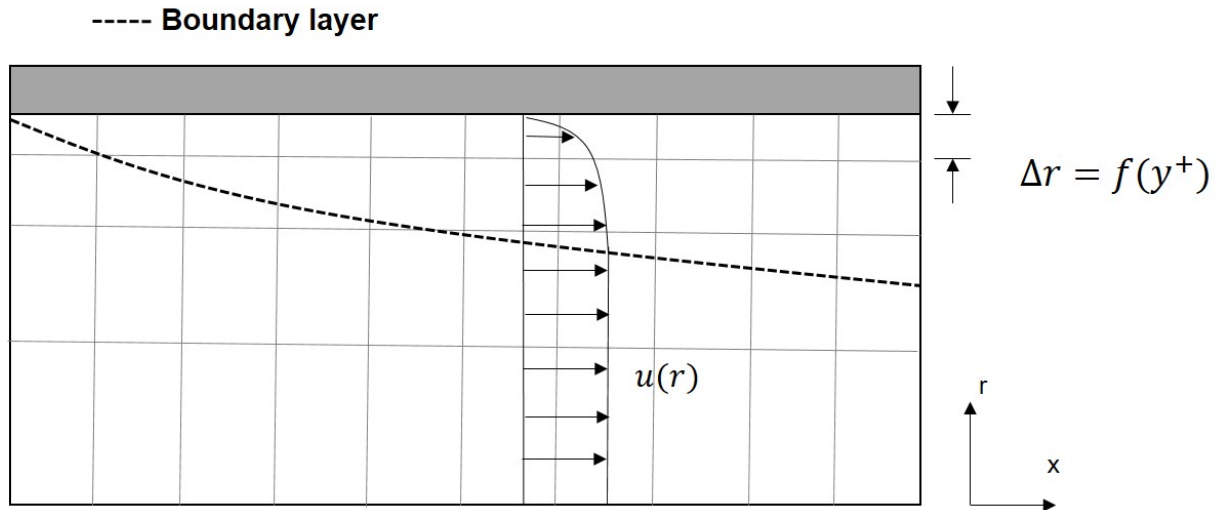
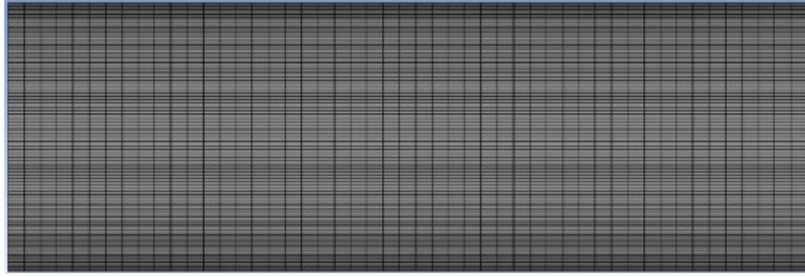


Figure 20 represents the computational mesh built to solve the method adopted by this study. We also adopted the refinement near the symmetry axis due to the high gradients and recirculation regions caused by swirling flow, as demonstrated in the literature review.

3.4.2 Mesh independence study

The goal of the mesh study is to eliminate the dependence of the result on the mesh. There are several ways to perform a mesh independence study. Here, the GCI (Grid Convergence Index) method is used (CELIK (2008)). The first step in using the GCI mesh independence method involves identifying the dimensionality of the computational domain,

Figure 20 – Mesh refinement near the wall (Source: Personal collection)



which in this study is two-dimensional. The variables used for mesh validation were drag coefficient (C_D) and tangential velocity (V_θ), the results are presented in table 4 and 5.

Table 4 – Grid Convergence Index for tangential velocity $Re = 4.9 \cdot 10^4$

Mesh	Elements	Refinement factor	$V_{\theta(5D)}$	GCI	Asy
-	-	-	[m/s]	[%]	-
M_3	180,000	-	1.786	-	-
M_2	240,000	1.16	1.748	2.711	-
M_1	375,000	1.25	1.723	0.9368	0.986
Extr.	-	-	1.71	-	-

Table 5 – Grid Convergence Index for drag coefficient $Re = 4.9 \cdot 10^4$

Mesh	Elements	Refinement factor	$C_{D(5D)}$	GCI	Asy
-	-	-	[m/s]	[%]	-
M_3	121,420	-	0,5772	-	-
M_2	267,901	1.485	0.5586	0.4847	-
M_1	527,420	1.403	0.5567	0.07014	0.9967
Extr.	-	-	0.5584	-	-

The intermediate meshes showed good GCI results and were used for the development of the study.

In this study we adopted as limit $GCI < 5$, so the intermediate or refined mesh that presents GCI within the stipulated is suitable for application of the simulations ensuring the independence of the error reported to the mesh. One should also ensure the value of $Asy = 1$, which reports the convergence of ϕ to an extrapolated value, having then an asymptotic convergence. The algorithm for solving the method was applied with the aid of the commercial tool EES (Engineering Equation Solver).

3.4.3 Boundary conditions and pre-processing

Boundary conditions must be specified to solve the set of equations. In the solid regions (pipe walls and tail) the no-slip condition is specified. The flow is assumed to be axisymmetric on the centerline. The cyclic boundary condition is assumed in the (θ)

direction. This implies that there are no gradients in the circumferential direction, but there may be circumferential velocity. At the inlet, the axial velocity and tangential velocity have been specified while the radial velocity is zero. At the output, pressure is specified considering radial pressure gradient.

After the mesh generations the boundary conditions of the computational domain are defined, to the pipe and tail walls are added the non-slip conditions (zero velocity). The symmetry axis imposes the condition of non-variation with respect to θ of the variables. At the inlet the uniform axial velocity and tangential velocity profiles are used, the radial velocity is zero. At the outlet the radial pressure gradient condition is non-zero, assuming the presence of the tangential velocity component at the outlet, where ρ is the density of the working fluid. These definitions are presented mathematically in table 6.

Table 6 – Boundary conditions

Inlet (x=0 m)	Wall	Symmetry	Outlet (x=3.375 m)
$u = u_0 = 2.7353 \frac{m}{s}$	$u = v = w = 0$	$\frac{\partial}{\partial \theta} = 0$	$\frac{\partial p}{\partial r} = \frac{\rho w^2}{r} \frac{Pa}{m}$
$v = v_0 = 0 \frac{m}{s}$	-	-	$\frac{\partial u}{\partial x} = 0$
$w = w_0 = 2.7353 \frac{m}{s}$	-	-	-

The flow properties and geometric values of the control domain are presented in table 7. The working fluid used for the simulations was water at a reference temperature of 25°C.

Table 7 – Properties

Property	Value
Density	998.2 $\frac{kg}{m^3}$
Viscosity	0.001003 $\frac{kg}{ms}$

3.4.4 Convergence

The process of numerical solution is executed until it reaches a predefined criterion, for this iterative methods are used that lead to convergence. There are several criteria to reach convergence, the most used in numerical methods are Jacobi and Gauss-Seidel (FORTUNA, 2000). Ansys Fluent uses the following criterion :

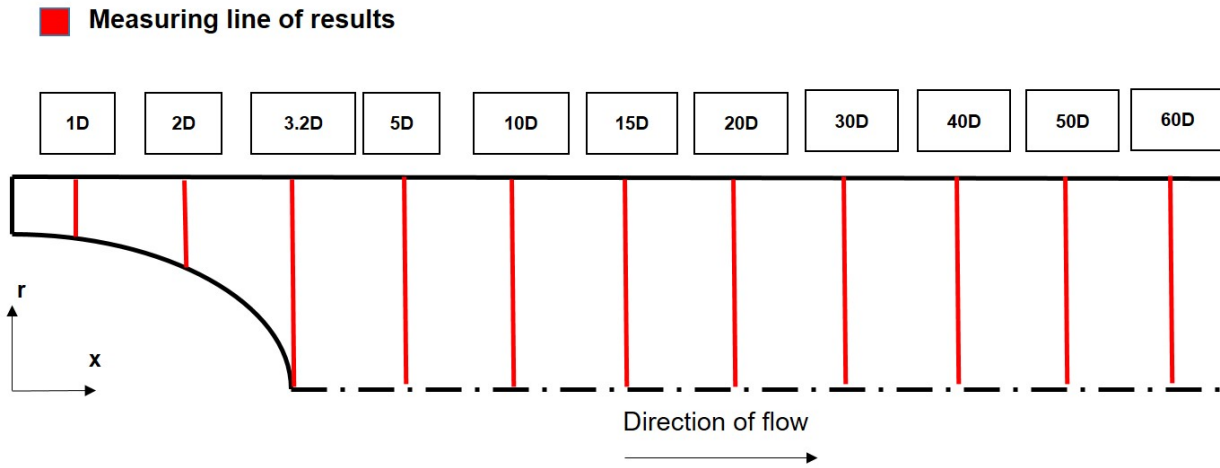
$$R^\phi = \frac{\sum_{cellsp} |\sum_{nb} a_{nb} \phi_{nb} + b - a_p \phi_p|}{\sum_{cellsi} |a_p \phi_p|} \quad (3.42)$$

this criterion is pressure-based, in which R_ϕ is the residual, P represents the cells of the computational domain, ϕ is the variable used for convergence, b is the constant part of the source term, a_p the center coefficient, a_{nb} are influence coefficients for neighboring cells.

For the momentum equations, the denominator term $a_p \phi_p$ is replaced by $v_p \phi_p$, where v_p is the magnitude of the velocity in cell P.

Four sections of the computational domain were selected to apply the convergence criteria, namely: 5D, 10D, 15D, 20D and outlet, as shown in figure 21. The average of the tangential velocities in the sections was used as the convergence variable. The other sections presented in the figure are used for post-validation analysis.

Figure 21 – Results Measurement Guidelines (Source: Personal collection)



It is assumed that the simulation is converged when the curves of the variation of the swirl velocity per iterations reach the plateau, i.e., present a stable flow. As each mesh may require a different flow time to achieve convergence, the convergence condition tool was used with a stopping criterion of 10^{-6} for the four sections analyzed. It is worth remembering that because it is a transient flow, in the first iterations the value of the variables will remain null until the flow reaches the sections, so it becomes necessary to enable the option time step before, entering the estimated value of iterations for the flow to reach the first session (5D). In this case the value used was 10000 iterations. In table 8, the residue values are described according to each variable.

Table 8 – Numerical residuals

u, v and w	10^{-4}
Conservation of mass, Reynolds Tensors, k and ε	10^{-5}

For convergence in the steady state with k- ε model, the convergence of the tangential velocity through the iterations reaching plateau obtained from the fluent is illustrated in figure 22.

Figure 23, which shows the continuity of the simulation for a more complete turbulence model in the transient regime, shows a correction of the velocities as the flow develops.

Figure 22 – Convergence of the solution in steady state (Source: Personal collection)

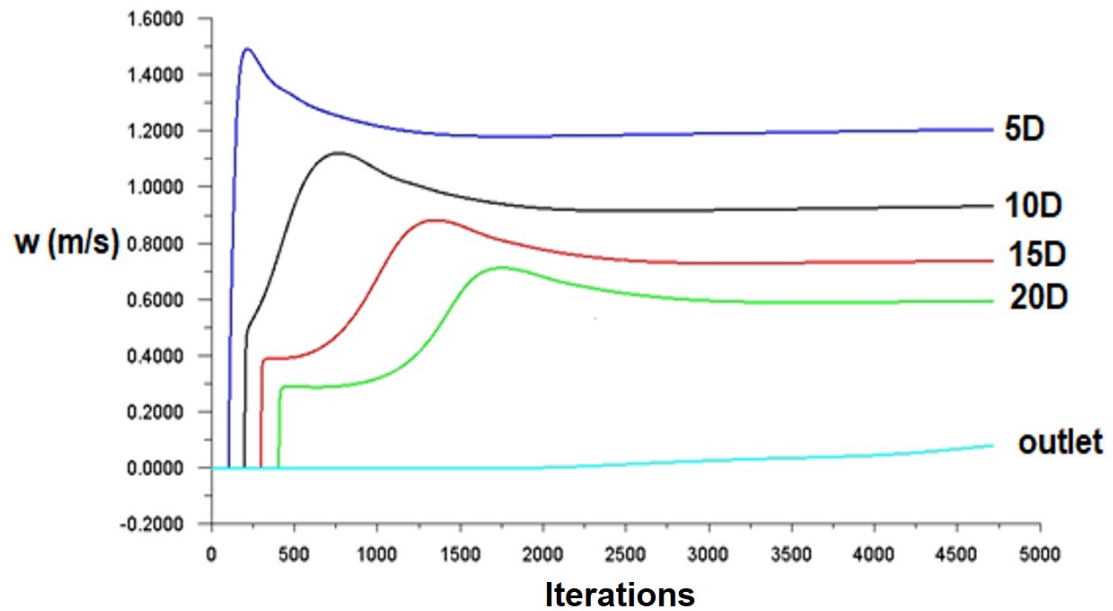
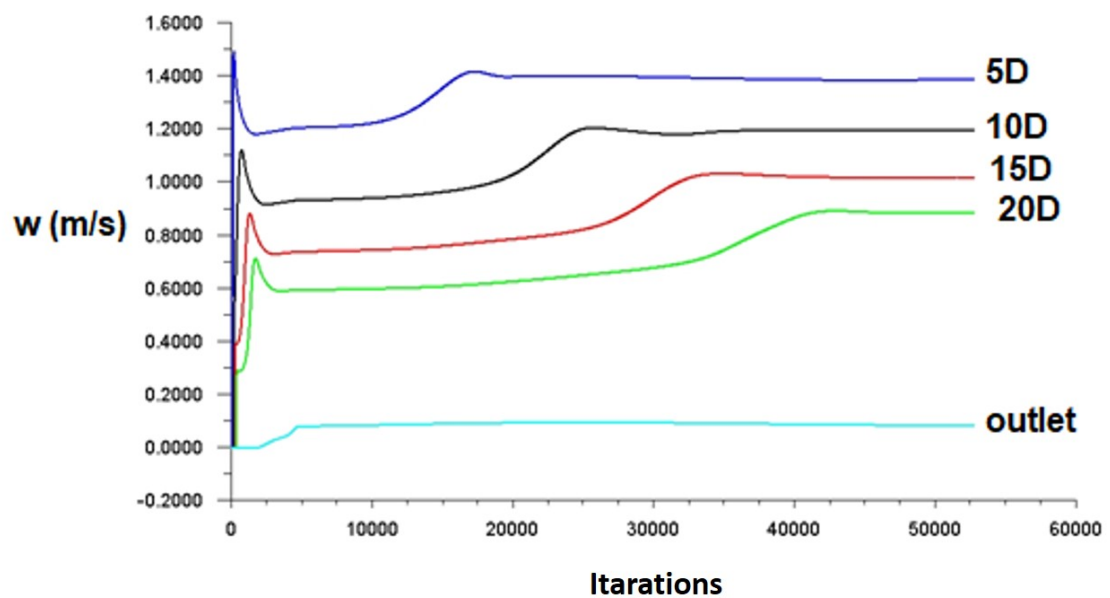


Figure 23 – Convergence of the solution in transient (Source: Personal collection)



4 Numerical validation

4.1 Introduction

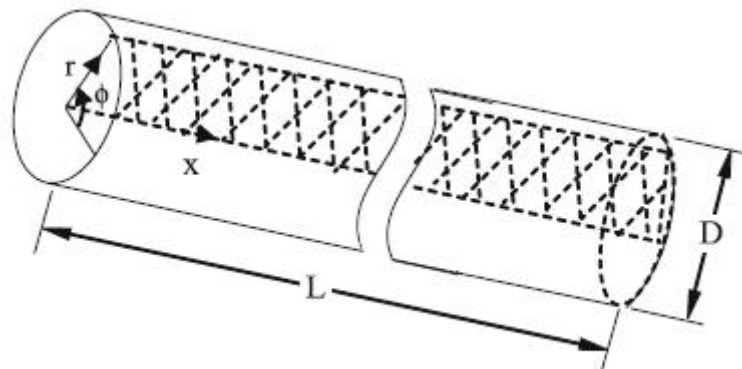
Numerical validation is a fundamental step in this study because it ensures the reliability of the simulated results with the real physical phenomena. In this chapter two validations will be presented: one for laminar flow with swirl (section 4.2) and another for turbulent flow (section 4.3).

4.2 Laminar validation with swirl

The first numerical validation is performed considering laminar flow with swirl. Although this flow regime is not the main focus of this study, the absence of closure models makes the validation process simpler. This simplicity is used as a gain of experience for the author.

For the validation of laminar flow we used the numerical study performed by Ayinde (2010), the author developed the study "A generalized relationship for swirl decay in laminar pipe flow". Ayinde performed a numerical study of laminar flow with swirl in a pipe, 80 mm in diameter and 6.4 m long, considering three-dimensional axisymmetric flow and obtained axial and tangential velocity profiles at different transverse positions. For this, the author considered, at the input of the computational domain, a tangential velocity superimposed by Poiseuille flow. The tangential component is formed by a combination of forced vortex in the center of the tube and free vortex in the annular region. The boundary conditions at the inlet were defined as:

Figure 24 – Computer domain Ayinde (Source: Ayinde (2010))



$$U(0, r, \phi) = U_{max} \left[1 - \left(\frac{r}{R} \right)^2 \right] \quad (4.1)$$

$$V(0, r, \phi) = 0 \quad (4.2)$$

$$W(0, r, \phi) = \begin{cases} W_{max} \frac{r}{r_{trans}}, & r < r_{trans} \\ W_{max} \frac{r_{trans}}{r} \left[\frac{R-r}{R-r_{trans}} \right], & r \geq r_{trans} \end{cases} \quad (4.3)$$

where r_{trans} is the transition radius between the free vortex and the forced vortex and U_{max} and W_{max} are maximum axial and tangential velocities respectively. R is the radius of the tube.

The boundary conditions imposed for solving the flow is the no-slip wall condition, i.e. $u=v=w=0$ and zero gauge pressure at the exit of the domain. Due to the symmetry methodology adopted by the author, the derivatives with respect to θ is zero.

The velocity profiles used for comparison with the results given by the author were the axial velocity and tangential velocity, for a Reynolds number at the inlet of 1000, number of turns at the inlet (S_0) equal to 1 and $r_{trans} = 60$ mm. The sections used to extract the results were the same presented by the study, given by x/D , they are: 0, 10, 20, 40 and 80.

The figures 25 and 26 show the axial velocity profiles and the tangential velocity profiles, respectively, for $Re = 1000$, $S_0 = 1$ and $r_{trans} = 0.75$.

It can be observed from figures 25 and 26 a good agreement between the results. The largest error found in the axial velocity profiles was for the maximum axial velocity at section 10D, with an error of 1%. As for the tangential velocity profiles, the largest error found was 3% for the maximum tangential velocity at section 40D.

In addition to the velocity profiles, the swirl number decay was used, given the importance of the variable for the study. The definition of S used by this study is given by (Bali 1998, Parchen Steenbergen 1998). Being:

$$S = \frac{2\pi \int_0^R U(rW)rdr}{\pi R^3 U_{avg}^2} \quad (4.4)$$

Figure 27 shows the swirl decay for two different Reynolds number ($Re = 1000$ and $Re = 1800$) and $S_0 = 1$.

Again, good agreement between the data can be observed. The largest error found for the swirl number decay was for the 10D section, with 17% error. To obtain the number of turns it is necessary to integrate the values of the axial velocity and tangential velocity profiles, according to equation 4.4. Thus, the greater difference in relation to the velocity

Figure 25 – Axial velocity profile (Source: Ayinde (2010))

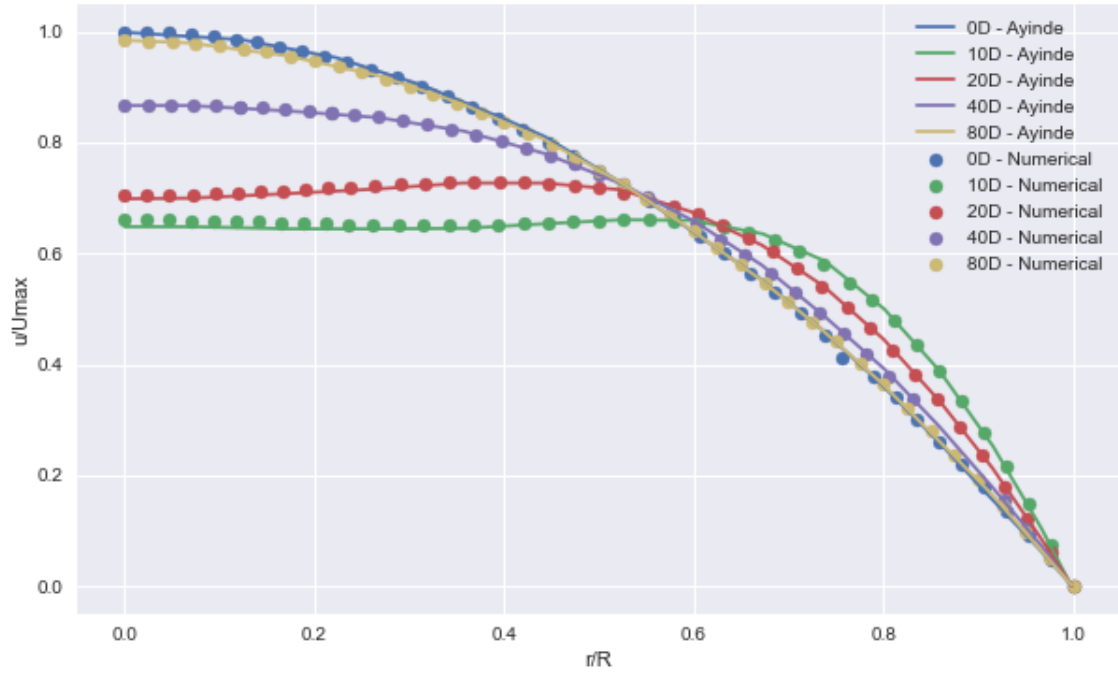


Figure 26 – Tangential velocity profile (Source: Ayinde (2010))

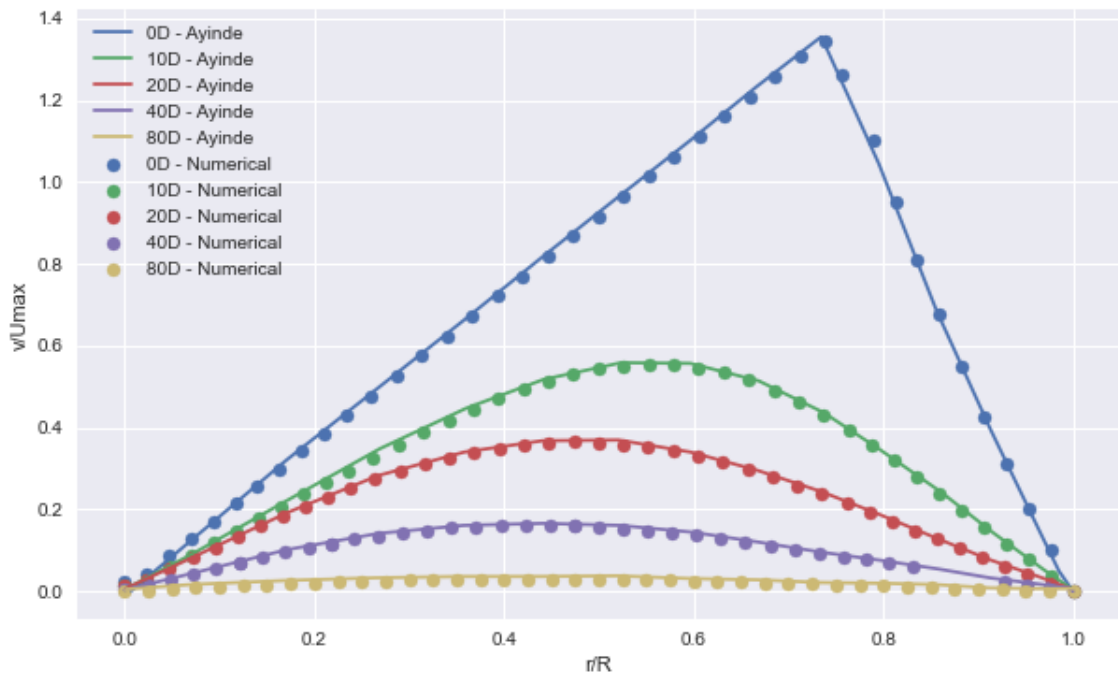
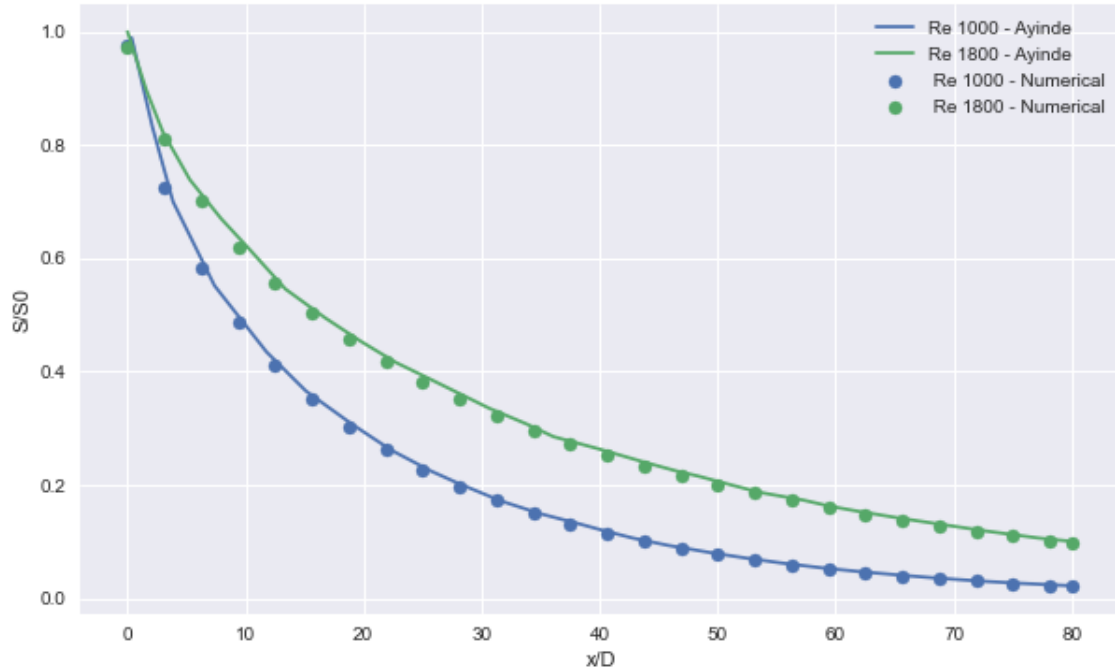


Figure 27 – Swirl number decay (Source: Ayinde (2010))



profiles can be explained by the accumulated error in the integration of the velocity profiles. The larger difference in relation to the velocity profiles can be explained by the accumulated error in the integration of the velocity profiles.

4.3 Turbulent validation with swirl

To validate the turbulent study, the work done by Dirkzwager (1996) was used. The author developed a study named “A new Axial Cyclone Design for Fluid-Fluid Separation”, where experimental data from the field of a single-phase and incompressible flow, with the working fluid being water, were presented. The results obtained by the author were used for validation, although the experimental study has a better representation in a real 3D modeling. The goal of this validation is to ensure that the 3D axisymmetric methodology adopted by this study has a good physical approximation and can be used for flow analysis with a lower computational cost.

The case used for validation was a flow deflected by a swirler with 45° , $Re_b = 4.9 \cdot 10^4$ and a temperature of 18.5°C . Velocity profiles were obtained using the two-dimensional LDA (Laser Doppler Anemometry) technique. The geometry of the zone setting has a diameter of 50 mm and a length of 3.375 m. The sections analyzed for the validation methodology were 5D, 10D, 15D and 20D, where D represents the tube diameter and has

a constant nominal value of 50 mm.

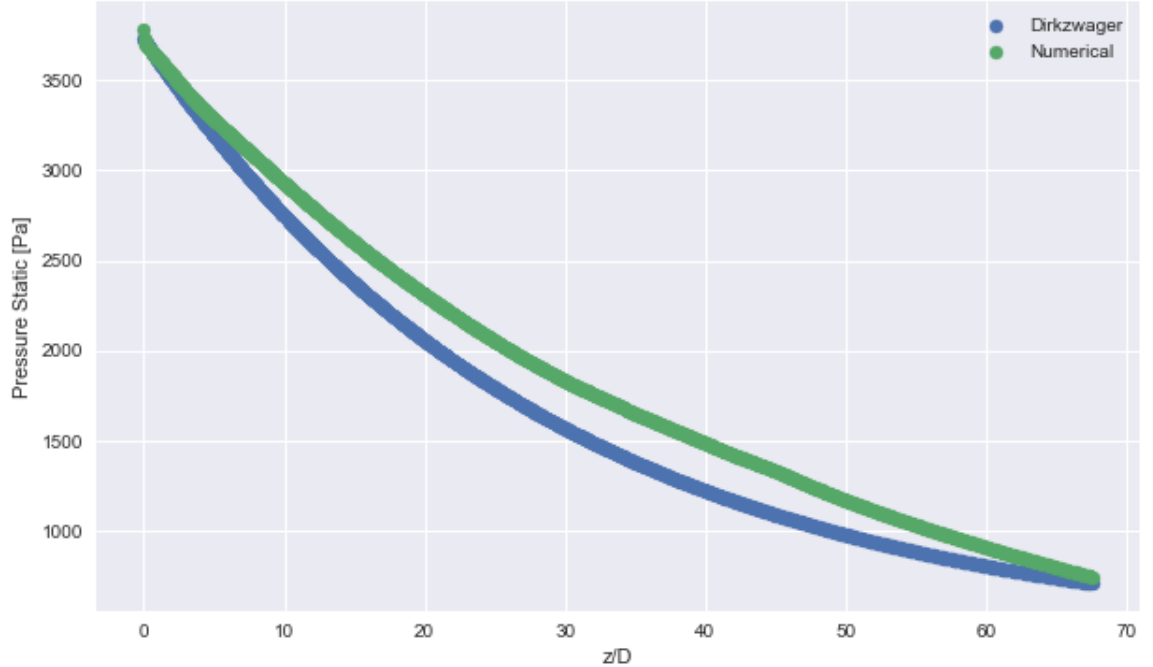
4.3.1 Axial static pressure

Experimental data from the distribution of static pressure on the tube wall given by Dirkzwager (1996) was used, the author also proposed an analytical expression given by the equation 4.5 as a function of length.

$$p = A + Be^{-C\frac{z}{D}} \quad (4.5)$$

Where, $A=389$ Pa, $B=3337$ Pa and $C=0.03467$ are coefficients of the equation and z/D the axial position. It can be seen in figure 28 that, when developing axially, the flow presents an exponential pressure drop, as shown by equation 4.5. This drop can be explained by the ratio of dissipation of axial momentum and tangential momentum.

Figure 28 – Static pressure on the wall (Source: Personal collection)



From a simplification of the momentum equation, assuming that the radial velocity in terms of physical magnitude is expressly smaller than the tangential velocity and the axial velocity, and that the gradient of the flow properties axially is considerably smaller than the radial gradient. To simplify the analysis, disregarding the viscous terms and

turbulent stresses, we have the following equations for the radial moment and axial moment (DIRKZWAGER, 1996):

$$P(r, z) = P(R, z) - \rho \int_r^R \frac{W^2}{r} dr \quad (4.6)$$

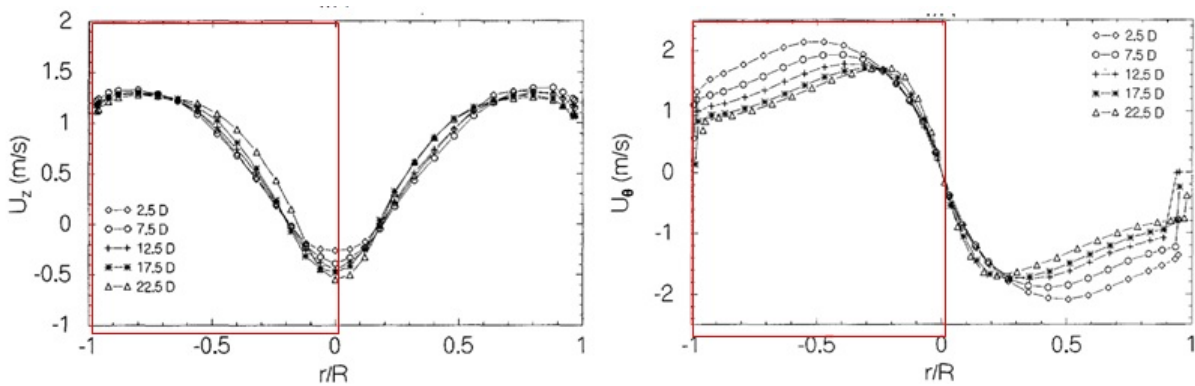
$$U \frac{\partial u}{\partial z} = -\frac{1}{\rho} \frac{\partial p}{\partial z} \quad (4.7)$$

From the 4.6 and 4.7 equations, it is observed that the axial pressure gradient is proportional to the axial velocity and the tangential velocity, which explains the decay with the flow development.

4.3.2 Velocity field

In inlet used the axial velocity, tangential velocity, and radial velocity profiles, which are represented algebraically by the equations 4.8 to 4.10 (DIRZWAGER 1996). The inlet of the computational domain adopted by this study, to obtain the numerical results, represents the first measurement section of Dirzwager's work, i.e., equal to 2.5D. The profiles presented by the author has a radial distribution of axial and tangential velocities throughout the pipe diameter, as shown in figure 29. The highlighted sections in the image represent the radial experimental data extraction area for use in this study due to the axisymmetric approach.

Figure 29 – (a) Axial velocity profile (b) Tangential velocity profile (Source: Dirkwager (1996))



The profile data were added to the computational domain of this study from a C code via the UDF (User Defined Function) tool from the Ansys Fluent package. In equations 4.8 to 4.10 the algebraic equations representing the axial velocity and tangential

velocity profiles are presented.

$$u(r) = 1.5367 \times 10^9 r^6 - 5.4451 \times 10^8 r^5 + 5.5862 \times 10^7 r^4 - 2.0496 \times 10^6 r^3 + 2.9047 \times 10^3 r^2 - 36.240r - 0.2704 \quad (4.8)$$

$$v(r) = 0 \quad (4.9)$$

$$w(r) = 3.6587 \times 10^{11} r^6 - 2.7841 \times 10^{10} r^5 + 8.1826 \times 10^8 r^4 - 1.1983 \times 10^7 r^3 + 1.0295 \times 10^5 r^2 - 6.1237 \times 10^2 r + 1.8108 \times 10^{-2} \quad (4.10)$$

4.3.2.1 Tangential velocity

The tangential velocity field is a primary output for analysis of swirling flow, it is what governs the characteristic behavior, e.g., of the vorticity, swirl intensity, and design parameters of a hydrocyclone. As presented in the literature review section, the tangential velocity profiles is a combination of forced vortex and free vortex. Figure 30 shows the radial distribution of tangential velocity for four downstream sections of the hydrocyclone, namely 5D, 110D, 15D, and 20D.

The tangential velocity field over the entire computational domain can be visualized by figure 31, including the transitions regions and behavior of the swirl decay.

In section 5D it can be seen that there is a ratio between solid body rotation and free vortex towards the pipe wall. As the flow develops axially, it is observed that the core of the solid body rotation decreases its radial size, with this there is a displacement of the peak maximum velocity towards the center of rotation, with a radial displacement of approximately 7.5 mm. The magnitude of the maximum velocity also decreases as the flow develops, with a lag of approximately 0.5 m/s from section 5D to section 20D. One can also analyze from the average axial vorticity, which is given by (WHITE, 2010):

$$\Omega_z = \frac{1}{r} \frac{\partial}{\partial r} (rw) \quad (4.11)$$

That is, for tangential velocity profiles closer to the exit of the fixed vanes that impose the swirling flow, there is a higher average vorticity due to the high radial gradient of tangential velocity and presence of forced vortex, with the development of the flow the vorticity decreases proportionally. This behavior is directly related to the dissipation of viscous effects due to friction with the wall. There is a production of shear stress, where the term $\langle vw \rangle$ is a source term in the tangential momentum equation and most important in

Figure 30 – Tangential velocity (Source: personal collection)

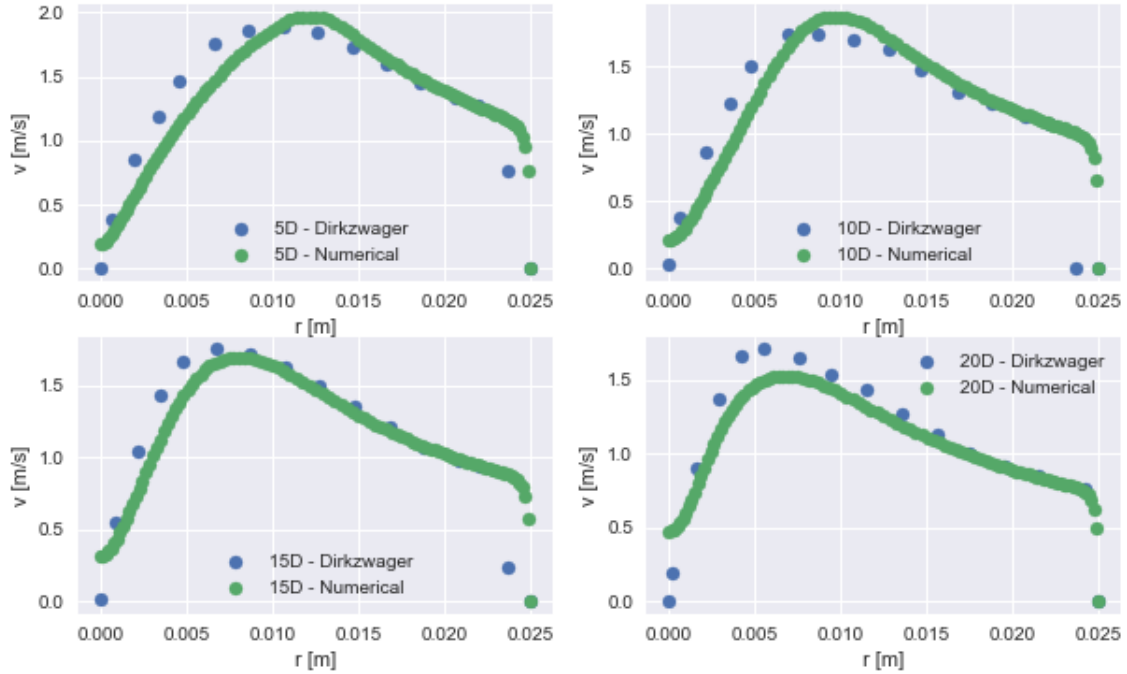
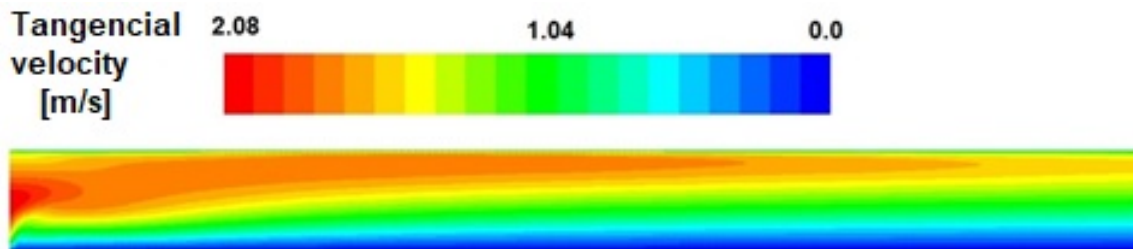


Figure 31 – Tangential velocity field (Source: personal collection)

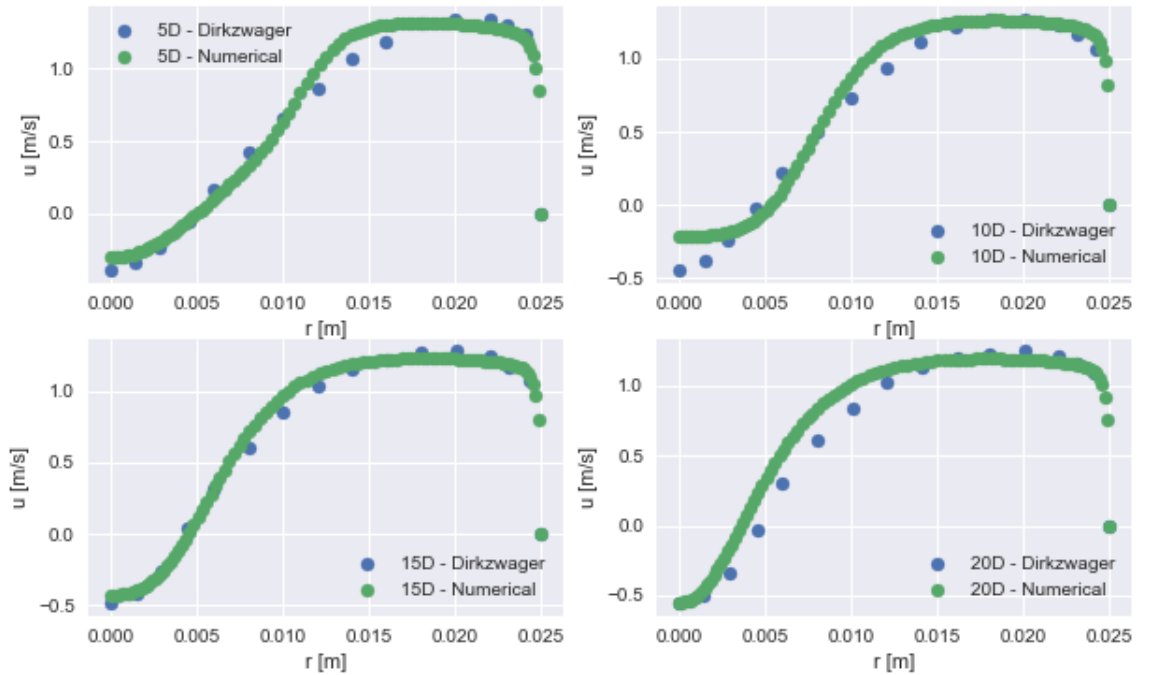


flow with swirl (OHTSUKA, 1995). The numerical results obtained by this study showed similar behavior to that presented by Dirkwager (1996), with some differences in specific regions, for all sections it is noted a greater proximity of the experimental results near the wall, which can be explained by a good modeling adopted for the wall law and prediction of viscous effects. In some points dominated by the forced vortex, there are small divergences, which can be explained by the high diffusivity of the swirling flow, and prediction of the quantity of motion tensors, especially the tensor $\langle vw \rangle$. Due to the forced vortex formation near the axis of symmetry and a radial pressure gradient in the same direction there is the formation of the core of the precession vortex and a higher concentration of mass in relation to the region near the wall.

4.3.2.2 Axial velocity

Figure 32 presents, in the same sections previously analyzed, the axial velocity profiles. Note that for all sections there are negative velocity values near the axis of rotation of the flow, this effect can be explained due to the high radial and axial pressure gradient (LILLEY, 1977). The regions of negative velocity are regions of recirculation in the flow, near the center of rotation there is the formation of a forced vortex that has a behavior of rigid body rotation, this causes a high adverse pressure gradient on the central line, i.e., the region of axial recirculation is linked to the stretching of the vortex. With the decay of the swirl, due to viscous effects, the recirculation region tends to disappear and the velocity profiles develop axially.

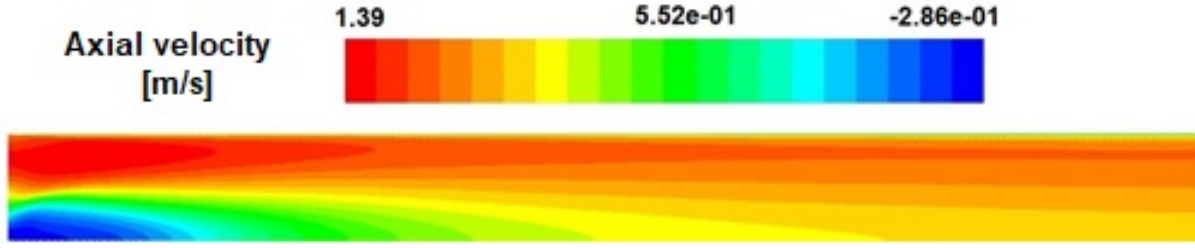
Figure 32 – Axial velocity (Source: personal collection)



The axial velocity field over the entire computational domain can be visualized by figure 33, including the transitions and negative axial velocity regions.

The results obtained numerically presented a greater proximity in the different axially distributed regions compared to the results of tangential velocity, as the tensors of the momentum equation have good prediction for the adopted modeling, the main one being the tensor $\langle uv \rangle$. It was also observed the axial velocity profiles near the outflow in order to make sure of the full development of the flow, as shown in figure 33. Another approach used for velocity field validation is the axial velocity profile developed close to

Figure 33 – Axial velocity field (Source: personal collection)

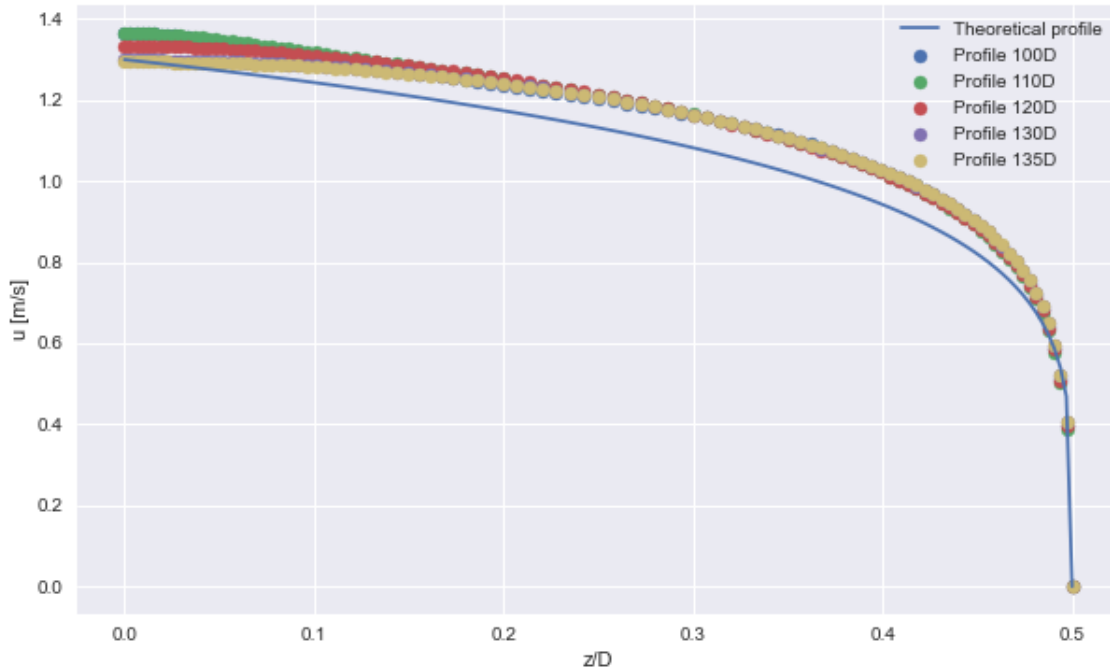


the computational domain output. Thus, the axial velocity profiles in the sections close to the exit were compared with a theoretical profile given by (WHITE, 2010):

$$u \approx U_0 \left(1 - \frac{r}{R}\right)^{\frac{1}{5}} \quad (4.12)$$

Where U_0 is the uniform axial velocity at the inlet. Figure 34 shows the developed axial velocity profiles, with 67.5D being the output section of the domain.

Figure 34 – Axial velocity field (Source: personal collection)



4.3.3 Swirl number

The swirl number is a modeling that measures the swirling force of the flow, being a dimensionless number resulting from the ratio between the total flow of axial amount of

motion and tangential amount of motion. For this study the modeling from the definition of Kitoh (1991) was used. As analyzed in the axial and tangential velocity sections, due to viscous dissipation on the pipe wall with the development of the downstream flow, there are reductions in the axial velocity and tangential momentum of the flow. With this, it reflects in the decay of the swirl with the development of the flow as presented in table 9 with the largest error equal to 11%. Importantly, the error is associated with the prediction of the axial and tangential velocity profiles, taking into account the sum of errors of the ratio between the quantities of axial and tangential motion has good results for the adopted modeling.

Table 9 – Swirl number

	Experimental	Numerical	Error [%]
0D (inlet)	1.20	1.34	10.45
5D	1.06	1.14	7.02
10D	0.88	0.98	10.20
15D	0.81	0.84	3.57
20D	0.73	0.72	1.36

It is known from the literature that flows with swirl number above 0.6 are considered to be strongly swirl flows and have an exponential approximation (DIRKZWAGER,1996), this type of approach is indicated for turbulent flows as is the study material of this paper.

As analyzed by Yuan, S.P. and R.M. (1998) the good prediction of the swirl number results even with divergent regions of the axial velocity profiles, can be explained due to the ratio between two integrals with greater weight in the annular that was correctly predicted by numerical modeling and in regions near the wall, this because the turbulent modeling of the flow with Reynolds Stress Model calculates the anisotropic turbulent viscosity near the wall which brought good results and consequently swirl numbers close to the experimental.

The swirl number was the third result analyzed for validation, as it is paramount to measure the amount of angular motion of the flow thinking about separation. The three results analyzed presented a quantitative and qualitative representation of the numerical results compared to the experimental, the errors may be associated with the 2D modeling adopted compared to the experimental 3D results, taking into account the low computational cost of 2D modeling and symmetry adopted for modeling the results obtained are valid with the objective of the study, as also concluded by Murphy et al. (2007). This makes it possible to continue the modeling adopted to explore more characteristics of the flow, varying the geometry and studying the adopted boundary conditions.

5 Tail aerodynamic analysis

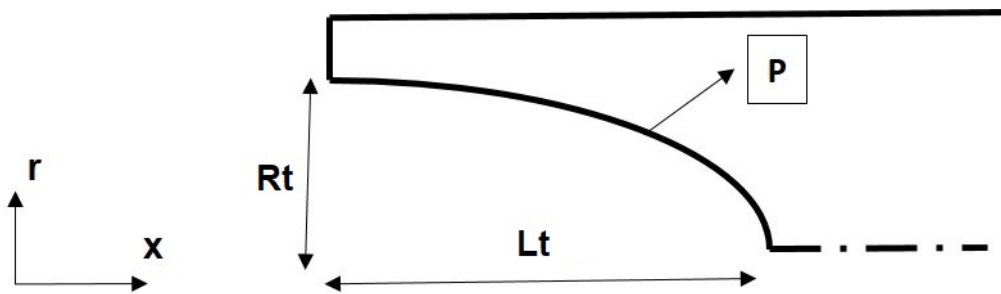
5.1 Introduction

The separation process, induced by the swirling flow, generates unwanted phenomena for effective application. Vortex Breaking Down, Processing Vortex Core and negative axial velocity regions, which are enhanced by turbulence, are phenomena that must be reduced or eliminated from the flow. One way to attack this problem is to introduce an aerodynamic tail at the entrance of the domain, where the swirl intensity is highest and these phenomena are present. The shapes of these tails are explored in the literature for application in axial hydrocyclones, onecognized by Dirkzwager (1996), Slot (2013) and Karimpoorheidari (2019). This section presents the tail modeling used for application in the present study, through the power law profile.

5.2 Aerodynamic Profile

The aerodynamic profile class selected for this study was the Power Series, used for rocket nose and other aerodynamically efficient applications with low drag coefficient (KRUNAL, 2019). The profile is given by a function where power accounts for the main body shape. Figure 35 shows a representation of the Power Series profile.

Figure 35 – Aerodynamic tail (Source: personal collection)



$$P(x, n) = R_t \left(\frac{x}{L_t} \right)^n \quad (5.1)$$

onde $0 \leq n \leq 1$

$$\begin{cases} n = 1 (Cone) \\ n = 0.75 \left(\frac{1}{4} Power \right) \\ n = 0.50 \left(\frac{1}{2} Power \right) \\ n = 0 \end{cases} \quad (5.2)$$

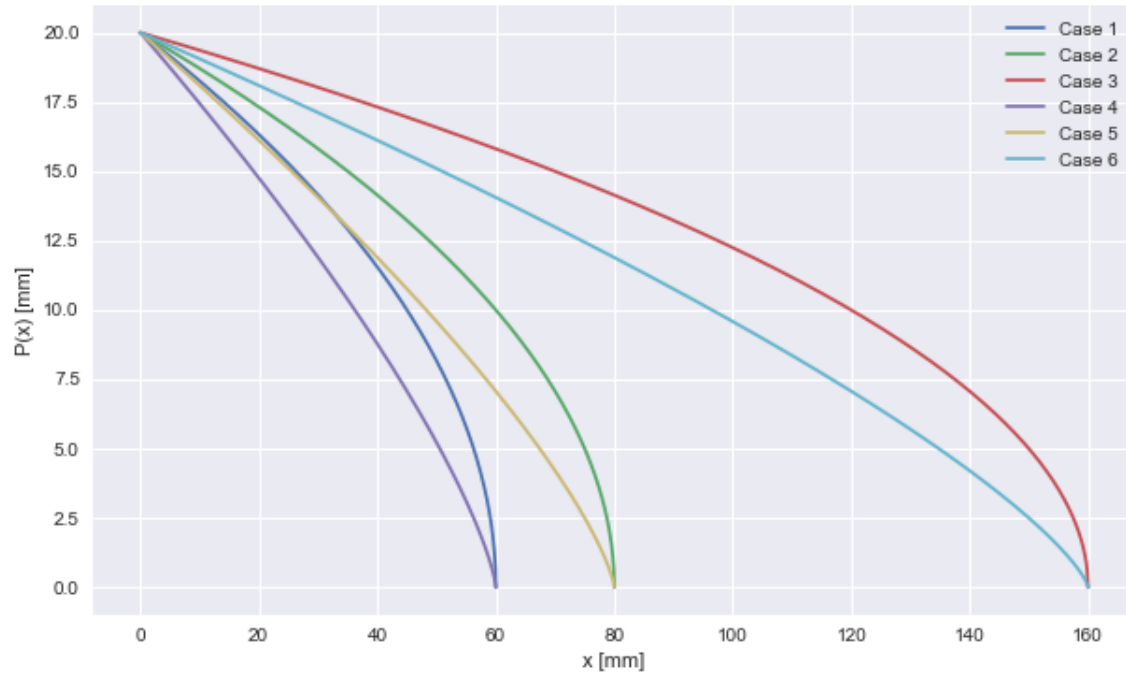
Profiles intermediate between cone and cylinder ($n=0.5$ and $n=0.75$) perform well for subsonic flows (CROWELL, 1996) and (KRUNAL, 2019). For each selected n the profile length $L=60$ mm, $L=80$ mm and $L=160$ mm was varied. These selected lengths are within the range used by Dirkzwager (1996) and Slot (2013). Table 10 presents the combinations used of each profile for simulation in the flow.

Table 10 – Cases Perfis Power Series

Case	1	2	3	4	5	6
n	0.5			0.75		
$L_t[mm]$	60	80	160	60	80	160

Figure 36 shows the plots of the curves of the profiles used.

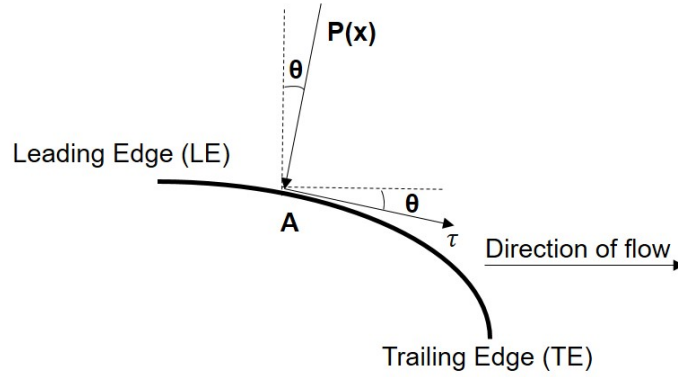
Figure 36 – Cases (Source: personal collection)



5.3 Theoretical Foundation

The drag coefficient was used to measure the best profile in relation to the lowest drag force. The equation 5.3 and 5.4 scales the drag from the forces represented in figure 37, where the forces due to static pressure (P) and shear stress (τ) are integrated in relation to angle across the surface (S) and area (A) of the airfoil (ANDERSON, 1991).

Figure 37 – Aerodynamic tail (Source: personal collection)



$$C_D = -2 \frac{\vec{F}_D}{\rho v^2 A} \quad (5.3)$$

$$F_D = \int_{LE}^{TE} (-p \sin \theta + t \cos \theta) dS \quad (5.4)$$

The trapezoids method was used to integrate the values of each discretization element, where a and b are the integration limits and h is the distance between the centroid of each element, according to equation 5.5 (BARROSO, 1987).

$$\int_a^b f(x) dx = \frac{h}{2} [f(x_0) + f(x_1)] \quad (5.5)$$

The tail is immersed in the flow, so the presence of this object generates greater pressure drop. With this, the pressure coefficient was used as another criterion for selecting the best profile. For incompressible and subsonic flows the Pressure Coefficient (C_P) is given by (ANDERSON, 1991):

$$C_p = \frac{p - p_\infty}{\frac{1}{2} \rho V_\infty^2} \quad (5.6)$$

Where the pressure variable is obtained from the quantity equations of motion of the simulations. The total pressure was used to calculate the pressure drop between the input sections of the computational domain and the tail end. Where is defined by:

$$p_0 = p + \rho \frac{V_\infty^2}{2} \quad (5.7)$$

However, the average of the total pressure in the area defined by the section was used for analysis, given by:

$$\bar{p}_0 = \frac{\int_A P dA}{\int_A dA} \quad (5.8)$$

The pressure drop is given by equation 5.9.

$$\Delta \bar{p}_0 = \bar{p}_{01} - \bar{p}_{02} \quad (5.9)$$

Where (\bar{p}_{01}) is average total pressure at the initial section and (\bar{p}_{02}) the average total pressure at the final measuring section.

5.4 Simulations

The 6 cases described in tables 4 and 5 were simulated to select the best aerodynamic profile, based on the lowest drag force and tangential velocity. The GCI mesh independence method was used to choose the number of elements used for all cases with the tail. The case used for applying GCI was index 3 with a tail length of 160 mm and $n=0.5$, chosen for having the longest tail length. From the analysis of the simulation data, the refined optimal mesh with 527.42 thousand quadrilateral elements with average dimensions of $4 \cdot 10^{-4}$ m was arrived at. The tables present data from application of the GCI, where simulations were performed in the turbulent regime with the RSM model and $y^+ = 7$. With the validation of the mesh, the same parameters were used for the other cases.

5.5 Results and selection

The results of drag, a variable used for selection of the airfoil, given by equation 5.6, are presented by table 11, with emphasis on the case of lowest drag value.

Table 11 – Drag coefficient values per case

Case	C_D
1	1.30
2	0.80
3	0.56
4	0.91
5	0.86
6	0.79

It is noted that increasing the length of the tail tends to decrease the value of the drag coefficient, and that the best shape for the lowest drag is for $n=0.5$. With this, case 3 was selected for continuity of the proposed studies. The pressure and shear stress coefficients were used to observe the influence of the airfoils on the flow, in figures 38 and 39 the results for the 6 cases are presented.

Figure 38 – Pressure coefficient (Source: personal collection)

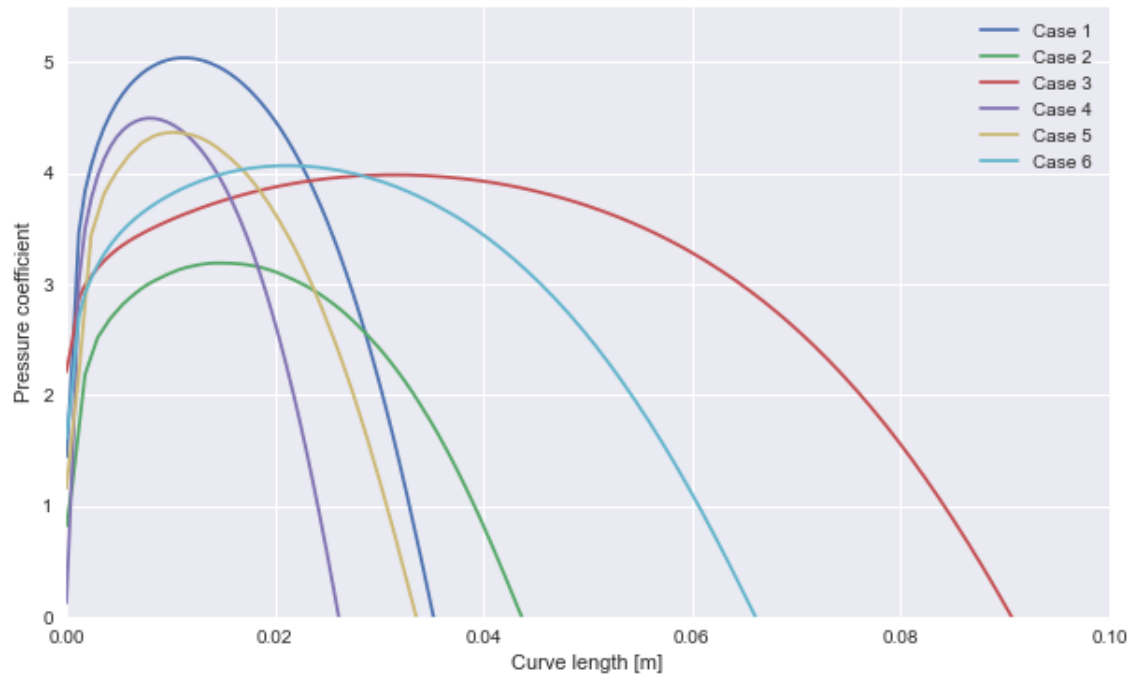
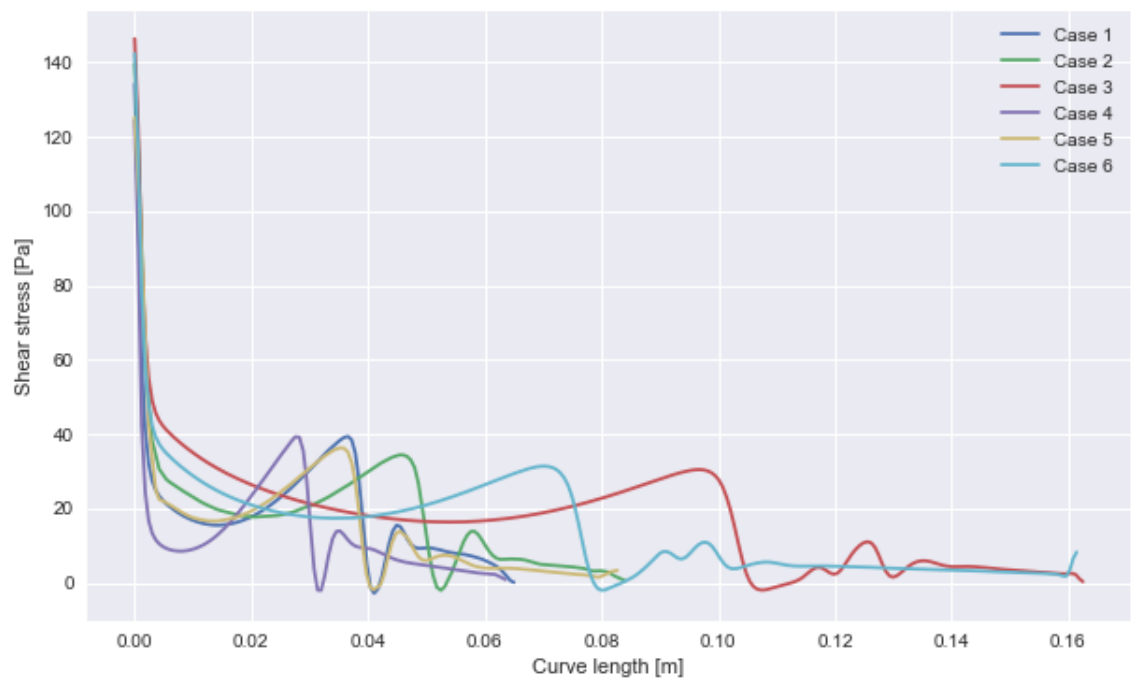


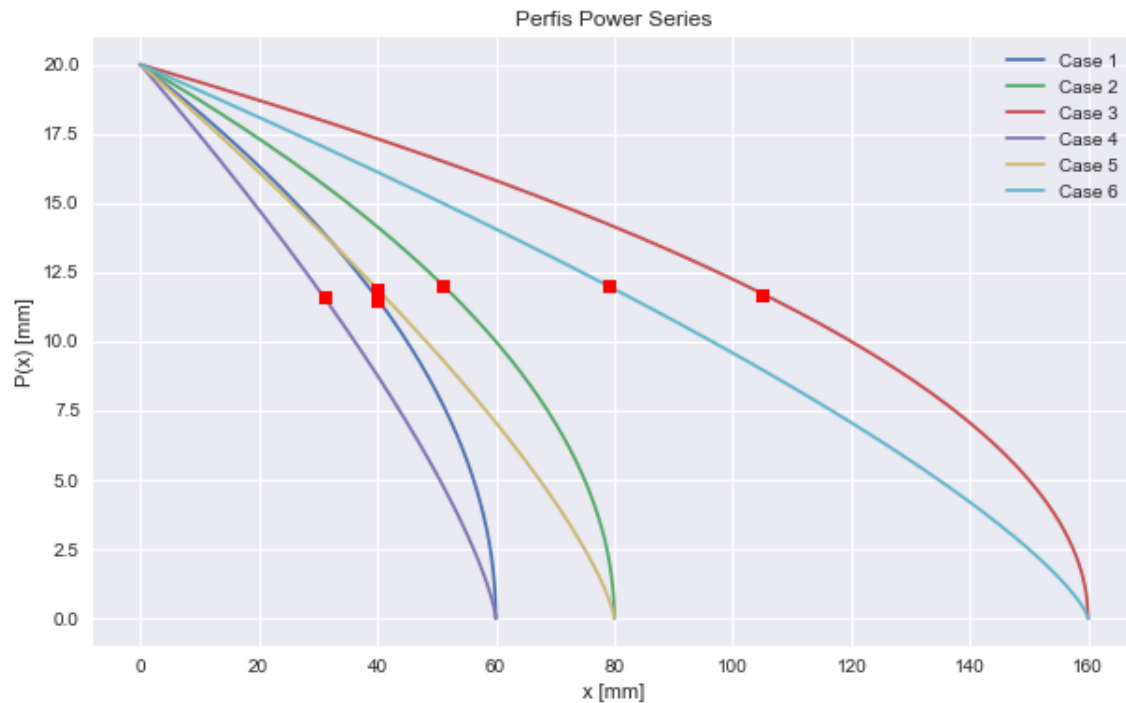
Figure 39 – Shear stress (Source: personal collection)



The pressure coefficient and shear stress assist in identifying the detachment of the boundary layer from the aerodynamic profile, the reversal of sign of the pressure coefficient demonstrates that there is an adverse pressure gradient, a phenomenon resulting from the detachment. Taken together, the detachment shows a sharp drop in shear stress from the point of separation, which can be noticed in both figures.

Similar behavior was observed for all tail profiles. The starting point of boundary layer separation was for $r=11$ mm for all cases, as per figure 40. An alternative for future studies is to optimize a profile to avoid or at least delay the boundary layer detachment.

Figure 40 – Boundary layer separation region (Source: personal collection)



After the analysis for selecting the profile, it was concluded that the best case for the application of this study is number 3, with a length of 160 mm, $n=0.5$.

6 Dynamics of a gas particle

6.1 Introduction

This chapter presents the mathematical modeling and numerical method used to describe the trajectory of a gas particle dispersed in a continuous water phase. The study aims to analyze the influence of flow properties for phase separation.

6.2 Mathematical formulation

For the computational modeling of the two-phase flow containing water with gas particles the Euler-Lagrange approach was used. This model treats the fluid phase as a continuum, solving the continuity and Navier-Stokes equations, while the dispersed phase is solved by tracing particles, bubbles or droplets in the calculated flow field. Particle interactions were neglected in this approach, where the dispersed phase occupies a low-volume fraction. Another simplification adopted for the model is the neglect of the particle influence on the flow as a whole, only the continuous phase alters the particle trajectory. To calculate the trajectory traveled, a balance of forces is applied from Newton's second law:

$$\frac{dv_p}{dt} = \vec{F}_D (\vec{u} - \vec{u}_p) + \frac{\vec{g}(\rho_p - \rho)}{\rho_p} + \vec{F} + \vec{G} \quad (6.1)$$

Equation 6.1 describes the variation of velocity by time of the particle, where v_p is the velocity of the particle, (\vec{F}_D) is the drag force due to the spherical shape of the particle, \vec{u} is the velocity of the continuous phase, \vec{u}_p is the velocity of the particle, \vec{g} is the force of gravity, ρ_p is the density of the particle and ρ is the density of the continuous phase. \vec{F} is the force due to virtual mass and \vec{G} is the force due to pressure gradient. The Reynolds of the particle being given by:

$$Re_p \equiv \frac{\rho d_p |\vec{u}_p - \vec{u}|}{\mu} \quad (6.2)$$

where μ is the kinematic viscosity of the continuous phase.

For turbulent flows the drag coefficient C_D is equal to 0.44. The drag force is given by:

$$F_D = \frac{18\mu}{\rho_p d_p^2} \frac{C_D Re_p}{24} \quad (6.3)$$

The force due to the virtual mass is given by:

$$\vec{F} = C_{vm} \frac{\rho}{\rho_p} \left(\vec{u}_p \nabla \vec{u} - \frac{d\vec{u}_p}{dt} \right) \quad (6.4)$$

where C_{vm} is the coefficient due to virtual mass and has value 0.5. The force due to the pressure gradient is given by:

$$\vec{G} = \frac{\rho}{\rho_p} \vec{u}_p \nabla \vec{u} \quad (6.5)$$

Note that the pressure gradient is larger for differences in densities between the continuous phase and dispersed phase.

6.3 Computer modeling of the trajectory

The modeling addressed in this study makes a discretization of the position (x_p, y_p) of the particle in each element of the computational mesh from an implicit scheme, where the new position of the particle is calculated through a trapezoidal discretization, given by the 6.6 and 6.7 equation.

$$x_p^{n+1} = x_p^n + \frac{1}{2} \Delta t (u_p^n + u_p^{n+1}) \quad (6.6)$$

$$\bar{y}_p^{n+1} = \bar{y}^n + c_1 \bar{k}_1 + c_2 \bar{k}_2 + c_3 \bar{k}_3 + c_4 \bar{k}_4 + c_5 \bar{k}_5 + c_6 \bar{k}_6 \quad (6.7)$$

where c_i and \bar{k}_4 are coefficient of the model given by Cash and Karp (1990).

7 Results and discussions

8 Conclusions and suggestions for future work

Conclusions

References

- ALGIFRI, A. H.; BHARDWAJ, R. K.; RAO, Y. V. N. Turbulence measurements in decaying swirl flow in a pipe. *Applied scientific research 4*: 233-250, 1988. Citado 2 vezes nas páginas 14 e 15.
- ARNOLD, K. *Petroleum Engineering Handbook*. [S.l.: s.n.], 2007. Citado 3 vezes nas páginas 15, 2 e 3.
- AYINDE, A. F. A generalized relationship for swirl decay in laminar pipe flow. *Vol. 35, Part 2, April 2010, pp. 129-137. © Indian Academy of Sciences*, 2010. Citado na página 13.
- BAKER, D. W.; SAYRE, C. L. Decay of swirling turbulent flow of incompressible fluids in long pipes. *Flow: its measurement and control in science and industry, volume no 1, PP.301-312*, 1974. Citado na página 11.
- BALI, T. Modelling of heat transfer and fluid flow for decaying swirl flow in a circular pipe. *International Communications in Heat and Mass Transfer, volume 25, no. 3, pp. 349-358*, 1998. Citado na página 16.
- CAMPEN, L. J. A. M. V. Bulk dynamics of droplets in liquid-liquid axial cyclones. *PhD thesis in Technology University Delft*, 2014. Citado 3 vezes nas páginas 9, 18 e 19.
- DELFO, R.; DIRKZWAGER, M. Motion of oil droplets in a strongly swirling pipe flow. *3th Internernational Conference on Multiphase Flow, Lyon, France*, 1998. Citado 3 vezes nas páginas 10, 18 e 19.
- DIRKZWAGER, M. A new axial cyclone design for fluid-fluid separation. *Ph.D. Thesis, Delft University of Technology*, 1996. Citado 5 vezes nas páginas 6, 10, 12, 18 e 19.
- ERDAL, F. M. et al. CFD simulation of single-phase and two-phase flow in gas-liquid cylindrical cyclone separators. *SPE Journal, Society of Petroleum Engineers (SPE)*, v. 2, n. 04, p. 436-446, dec 1997. Citado na página 20.
- FRANCIA, V. An experimental investigation of the swirling flow in a tall-form counter spray dryer. *Experimental Thermal and Fluid Science*, 2015. Citado na página 15.
- GUPTA, A. K.; LILLEY, D.; SYRED, N. Swirl flows. *Tunbridge Wells: ABACUS PRESS*, 1984. Citado na página 11.
- HANJALIC, K. Second-moment turbulence closures for cfd: Needs and prospects. *International Journal of Computational Fluid Dynamics, v12(1).*, pp. 67-97, 2018. Citado na página 5.
- HAYES, J. J. et al. Hydrocyclones for treating oily water: development and field testing in bass strait. *Proceedings of the 17th Annual Offshore Technical Conference, pp. 549-556*, 1985. Citado na página 10.
- HOEKSTRA, A. J. Gas flow field and collection efficiency of cyclone separators. *Technical University Delft, Stevinweg*, 2000. Citado 2 vezes nas páginas 4 e 15.

- HOEKSTRA, A. J.; DERKSEN, J. J.; AKKER, H. E. A. D. An experimental and numerical study of turbulent swirling flow in gas cyclones. *Chemical Engineering Science*, v. 54, p. 2055-2065, 1999. Citado 2 vezes nas páginas 16 e 17.
- HOFFMANN, A. C.; STEIN, L. E. Gas cyclones and swirl tubes. 2008. Citado 2 vezes nas páginas 15 e 10.
- HUANG, L. et al. Numerical analysis of a novel gas-liquid pre-separation cyclone. *Chem. Eng. Process.*, pp. 256-266, 2018. Citado 2 vezes nas páginas 15 e 4.
- JAWARNEH, A. M. et al. Enhancement of a cylindrical separator efficiency by using double vortex generators. *Energy Conversion and Management*, 2009. Citado 2 vezes nas páginas 16 e 17.
- KARIMPOORHEIDARI, A. A numerical study of swirl flow in pipes. *Master of Science, Delft University of Technology*, 2019. Citado 2 vezes nas páginas 18 e 19.
- KHODABANDEH, E. et al. CFD study of non-premixed swirling burners: Effect of turbulence models. *Chinese Journal of Chemical Engineering*, Elsevier BV, v. 28, n. 4, p. 1029–1038, apr 2020. Citado 2 vezes nas páginas 17 e 18.
- KITOH, O. Experimental study of turbulent swirling flow in a straight pipe. *Journal of Fluid Mechanics*, volume 225, pp. 445-479, 1991. Citado 4 vezes nas páginas 5, 11, 12 e 14.
- KIYA, M.; FUKUSACO, S.; ARIE, M. Laminar swirling flow in the entrance region of a circular pipe. *Bulletin of JSME*, Japan Society of Mechanical Engineers, v. 14, n. 73, p. 659–670, 1971. Citado na página 13.
- KREBS, T.; SCHROËN, K.; BOOM, R. Coalescence dynamics of surfactantstabilized emulsions studied with microfluidics. *Soft Matter*, (8):10650–10657, 2012. Citado na página 19.
- KUNDU, P. K.; COHEN, I. M. *Fluid Mechanics*. [S.l.: s.n.], 2008. Citado na página 12.
- LAVAN, Z.; NIELSEN, H.; FEJER, A. A. Separation and flow reversal in swirling flow incircular ducts. *Illinois Insti-tute of Technology, and Research Institute, Chicago*, no 9, pp 1747–1757, 1969. Citado na página 13.
- LIMA, A. A. de. Estudo numérico do escoamento ao redor de cilindros flexíveis. *Phd Thesis, University of São Paulo*, 2011. Citado 2 vezes nas páginas 15 e 12.
- LINDEN, A. J. T. Investigations into cyclone dust collectors. *Proceedings of the Institution of Mechanical Engineers*, v. 160, n. 1, p. 233–251, 1949. Citado na página 18.
- LIU, L.; BAI, B. NUMERICAL STUDY ON SWIRLING FLOW AND SEPARATION PERFORMANCE OF SWIRL VANE SEPARATOR. *Interfacial Phenomena and Heat Transfer*, Begell House, v. 5, n. 1, p. 9–21, 2017. Citado na página 20.
- LUCCA-NEGRO, O.; O'DOHERTY, T. Vortex breakdown: review. *Progress in Energy and Combustion Science*, 2014. Citado na página 15.
- MEIER, H.; MORI, M. Anisotropic behavior of the reynolds stress in gas and gas-solid flows in cyclones. *Powder Technology*, v. 101, n. 2, p. 108-119, 1999. Citado na página 17.

MURPHY, S. et al. Prediction of strongly swirling flow within an axialhydrocyclone using two commercial cfd codes. *Chemical Engineering Science*, volume 62, pp. 1619-1635, 2007. Citado 3 vezes nas páginas 5, 17 e 18.

NAJAFI, A. F. et al. Numericalanalysis of turbulent swirling decay pipe flow. *International Communications in Heatand Mass Transfer*, vol. 32, pp. 627-638, 2005. Citado na página 17.

NIEUWSSTADT, F. T.; DIRKZWAGNER, M. A fluid mechanics model for an axialcyclone separatora fluid mechanics model for an axialcyclone separator. *Industrial Engineering Chemical Research*, volume 34, pp. 3399-3404, 1995. Citado na página 10.

OJO, A. O.; ODUNFA, K. M.; OYEWOLA, O. M. Numerical simulation of the evolution of reynolds number on laminar flow in a rotating pipe. *American Journal of Fluid Dynamics*, 2014. Citado na página 12.

POPE, S. B. Turbulent flows. *Cambridge University Press*, 2000. Citado na página 4.

ROCHA, A. D. Estudo experimental e numérico de um escoamento com giro. *Phd Thesis, University of Campinas*, 2013. Citado na página 11.

ROCHA, A. D.; BANNWART, A. C.; GANZAROLLI, M. M. Numerical and experimental study of an axially induced swirling pipe flow. *International Journal of Heat and Fluid Flow*, 2015. Citado na página 11.

ROCHA, A. D.; BANNWART, A. C.; GANZAROLLI, M. M. Effects of inlet boundary conditions in an axial hydrocyclone. *Journal of the Brazilian Society of Mechanical Sciences and Engineering*, 2017. Citado na página 13.

SAVREE. Cyclone separator design, components and how it works. <<https://savree.com/en/product/cyclone-separator-working-principle-dust-separator/>>. Acesso em: 28 abr. 2020., 2020. Citado 2 vezes nas páginas 15 e 5.

SCHOLVIN, S. et al. Densidade, distância, divisão e as redes de produção globais: o caso do setor brasileiro de petróleo e gás. *Economia e Sociedade*, FapUNIFESP (SciELO), v. 29, n. 1, p. 85–119, apr 2020. Citado na página 1.

SILVESTER, N. R.; SLEIGH, M. A. Hydrodynamic aspects of particle capture by mytilus. *Journal of the Marine Biological Association of the United Kingdom*, Cambridge University Press (CUP), v. 64, n. 4, p. 859–879, nov 1984. Citado na página 13.

SINGH, M. P.; SINHA, P. C.; AGGARWAL, M. Swirling flow in a straight circular pipe. *ZAMM - Zeitschrift für Angewandte Mathematik und Mechanik*, 1980. Citado na página 13.

SLOT, J. J. Development of a centrifugal in-line separator for oil-water flows. *PhD thesis in University of Twente*, 2013. Citado 4 vezes nas páginas 3, 18, 19 e 20.

SMYTH, I. C.; THEW, M. T.; COLMAN, D. A. The effect of split ratio on heavydispersions in liquid-liquid separation in hydrocyclones. *Book of papers presented at the 2nd International Conference on Hydrocyclones, Bath England*, pp. 117-190, 1984. Citado na página 10.

- STEENBERGEN, W. Turbulent pipe flow with swirl. *Ph.D.Thesis, Technische Universiteit Eindhoven*, 1995. Citado 3 vezes nas páginas 12, 14 e 15.
- STEENBERGEN, W.; VOSKAMP, J. The rate of decay of swirl in turbulent pipe flow. *Flow Measurement and Instrumentation*, 1998. Citado 2 vezes nas páginas 15 e 12.
- STRAUSS, W. *Industrial Gas Cleaning: The Principles and Practice of the control of gaseous and particles emissions*. [S.l.: s.n.], 1975. Citado na página 18.
- SVAROVSKI, L. Hydrocyclones. *Tecnomic Publishing Co. Inc.*, 1984. Citado na página 10.
- SWANBORN, R. A new approach to the design of gas-liquid separators for the oil industry. *Civil Engineering and Geosciences*, 1988. Citado 2 vezes nas páginas 18 e 19.
- SYRED, N.; BEER, J. Combustion in swirling flows: a review. *Combustion and flame, Elsevier*, v.23,n.2,p.143-201, 1974. Citado na página 12.
- TALBOT, L. Laminar swirling pipe flow. *J. Appl. Mech.*, 1954. Citado na página 12.
- TRIGGIA. *Fundamentos de Engenharia de Petróleo. Rio de Janeiro. Interciência, Petrobras*. [S.l.: s.n.], 2001. Citado na página 1.
- TYVOLD, P. F. Modeling and optimization of a subsea oil - water separation system. *Master thesis , Norwegian University of Science and Technology*, 2015. Citado 2 vezes nas páginas 15 e 10.
- VERLAAN, C. Performance of novel mist eliminators. *Ph.D. Thesis, Delft University of Technology*, 1991. Citado 2 vezes nas páginas 18 e 19.
- WANG, B. et al. Numerical study of gas-solid flow in a cyclone separator. *Applied Mathematical Modelling*, Elsevier BV, v. 30, n. 11, p. 1326–1342, nov 2006. Citado na página 20.
- WILCOX, D. Journal of the brazilian society of mechanical sciences and engineering. *Journal of the Brazilian Society of Mechanical Sciences and Engineering*, 1998. Citado na página 16.
- YANG, J. et al. A new pressure drop model of gas-liquid cyclone with innovative operation mode. *Chem. Eng. Process.*, pp. 256-266, 2015. Citado na página 4.
- YANG, L. et al. Experimental and numerical study of separation characteristics in gas-liquid cylindrical cyclone. *Chemical Engineering Science*, Elsevier BV, v. 214, p. 115362, mar 2020. Citado na página 20.
- YAZDABADI, P. A.; GRIFFITHS, A. J.; SYRED, N. Characterization of the pvc phenomena in the exhaust of a cyclone dust. *Experiments in Fluids*, v. 17, p.84-95, 1994. Citado na página 14.